

University of Cincinnati

Date: 8/31/2012

I, James Russo, hereby submit this original work as part of the requirements for the degree of Master of Science in Mechanical Engineering.

It is entitled:

The Effects of Laser Shock Peening on the Residual Stress and Corrosion Characteristics of Magnesium Alloy AZ91D for use as Biodegradable Implants

Student's name: **James Russo**

This work and its defense approved by:

Committee chair: Dong Qian, PhD

Committee member: Seetha Ramaiah Mannava, PhD

Committee member: Mark Schulz, PhD

Committee member: Vijay Vasudevan, PhD



2950

**The Effects of Laser Shock Peening on the Residual Stress
and Corrosion Characteristics of Magnesium Alloy AZ91D
for use as Biodegradable Implants**

A Thesis Submitted to the
Division of Research and Advanced Studies
Of the University of Cincinnati
In partial fulfillment of the
Requirements for the degree of

Master of Science

in the School of Dynamic Systems
in the College of Engineering

2012

James A. Russo

BSME, University of Cincinnati, 2010

Committee Chair: Dr. Dong Qian

ABSTRACT

There is a continuing interest in exploring magnesium and its alloys for biomedical applications due to its low density and high strength properties that are very similar to bone. However, the high corrosion rate of magnesium and its alloys while immersed in body fluid restrict the material from use as permanent implants. The ability to control the corrosion rate of a material is an important factor in the development of biodegradable implants. An emerging topic of study for controlling the corrosion rates of different material is through imparting high levels of compressive residual stress on the surface. One effective process of imparting high levels of compressive residual stress on a material is Laser Shock Peening (LSP). Laser Shock Peening is a material process in which a high-pulsed laser creates a pressure shock wave that travels through the depth of the material, leaving high levels of compressive residual stress through its depth.

This thesis will present a study on the effects of compressive residual stresses imparted through laser shock peening on the corrosion characteristics of magnesium alloy AZ91D. In order to understand all aspects of this, an in-depth material characterization of the alloy is performed. Next, an LSP study is performed in which the optimal LSP parameters are determined. The experimental results are validated using Finite Element Analysis in LS-DYNA. Once LSP parameters have been optimized, corrosion tests are performed to link the relationship between compressive residual stress and corrosion rates of AZ91D.

ACKNOWLEDGEMENTS

I would like to thank Dr. Dong Qian, Dr. Vijay Vasudevan, Dr. Mark Schulz, and Dr. Seethia Mannava for serving on my thesis committee. I would like to extend a special thanks to Dr. Dong Qian for the opportunity to work under his guidance. I would also like to thank Dr. Seethia Mannava for the extra time and effort he spent working with me throughout this project. Thanks to John Yin for all of his help with experimental work. I want to acknowledge Abhishek Telang, Sagar Bhamare, James Guenes and Yixiang Zhao for their friendship and support throughout this project. Finally, I want to thank my friends and family for all of their support in my life.

Contents

ABSTRACT.....	ii
ACKNOWLEDGEMENTS.....	iv
List of Figures.....	viii
List of Tables.....	x
Chapter 1: Introduction.....	1
1.1 General Background.....	1
1.2 Literature Review.....	3
1.2.1 Stress Shielding.....	3
1.2.2 Magnesium as Biodegradable Implants.....	5
1.2.3 Brief History.....	5
1.2.4 Corrosion Resistance of Magnesium and Magnesium Alloys.....	6
1.2.5 Stress Corrosion Cracking (SCC) of Magnesium.....	7
1.2.6 Applications and Potential Benefits of LSP on Magnesium Alloys.....	8
1.3 Laser Shock Peening.....	9
1.3.1 Background.....	9
1.3.2 Physical Process.....	10
1.3.3 Temporal Shape.....	11
1.4 Objective.....	14
Chapter 2: Material Characterization.....	15
2.1 Microstructure Analysis.....	16
2.2 X-Ray Diffraction & Residual Stress Measurements.....	18
2.3 Hardness.....	22
2.4 Residual Stress Characterization.....	23
2.4.1 LSP Trial 1.....	23
2.4.2 LSP Trial 2.....	24
2.4.3 LSP Trial 3.....	25
2.5 LSP Characterization.....	27
2.5.1 Spatial Variation.....	27
2.5.2 Stress Depth Profile.....	28
2.5.3 Microstructure after LSP.....	30

2.5.4	Hardness after LSP	32
Chapter 3:	Finite Element Analysis Modeling and Simulation	33
3.1	Pressure Pulse Model	33
3.2	Material Model	36
3.3	FEA Model – Pre-processing	38
3.3.1	Meshing and Geometry	39
3.3.2	Boundary Conditions	40
3.3.3	Applied Loads	40
3.3.4	Damping	42
3.3.5	Runner Script	42
3.4	Post-processing	42
Chapter 4:	FEA Results	44
4.1	Material Model Parameter Study	44
4.2	Thermal Energy Conversion Factor (α) Variation Study	48
4.3	Finite Element Model Conclusions	50
Chapter 5:	Experimental Methods	52
5.1	DC Polarization Test	52
5.1.1	Theory	52
5.1.2	Methodology	54
5.1.3	Procedure	55
5.2	Immersion Corrosion Test	58
5.2.1	Theory	59
5.2.2	Methodology	59
5.2.3	Procedure	61
Chapter 6:	Experimental Results	64
6.1	DC Polarization Test Results	64
6.2	Immersion Test Results	66
Chapter 7:	Discussions	69
7.1	LSP Methods	69
7.2	Corrosion Tests	70
Chapter 8:	Conclusion and Future Work	72

References..... 75

List of Figures

Figure 1.1 – LSP configuration (from [22]).....	10
Figure 1.2 – Gaussian peak (from [22]).....	12
Figure 1.3 – Short rise time peak profile (from [22])	13
Figure 2.1 – AZ91 phase diagram (from [24]).....	16
Figure 2.2 – AZ91D microstructure as-received polished and etched (a) optical (b) SEM.....	17
Figure 2.3 – As-received polished and etched (a) AZ31 (b) pure magnesium	17
Figure 2.4 – LXR peak comparisons between (a) AZ31B (b) as-recieved AZ91D, and (c) AZ91D after annealing for 24 hrs. at 400°C	20
Figure 2.5 – XRD patterns (a) annealed and (b) as-received.....	21
Figure 2.6 – AZ91D after annealing for 24 hours at 400°C (a) SEM, (b) optical	22
Figure 2.7 – LSP trial 2 results	25
Figure 2.8 – 15mm x 100mm x 3.0mm coupon.....	26
Figure 2.9 – LSP trial 3 results	27
Figure 2.10 – Veeco spatial profiles.....	28
Figure 2.11 – Stress depth profiles.....	30
Figure 2.12 – XRD patterns of AZ91D before and after LSP	32
Figure 3.1 – LSP physical process	34
Figure 3.2 – Residual stress depth profile target for simulation	39
Figure 3.3 – Model Setup (a) meshed 3-D Model, (b) non-reflecting boundary conditions, (c) loads	40
Figure 3.4 – Pressure pulse time history (a) 5.42 GW/cm ² , 21.14 ns, (b) 1.71 GW/cm ² , 28.8 ns	41
Figure 4.1 – Stress-depth profile FEA model validation	46
Figure 4.2 – Residual stress of single shot, double sided LSP of (a) σ_x and (b) σ_y in MPa.....	46
Figure 4.3 – Through-depth residual stress (a) σ_x and (b) σ_y in MPa	47
Figure 4.3 – Dimple depth comparison.....	48
Figure 4.3 – Alpha pressure pulse variation	49
Figure 4.4 – Alpha variation stress-depth results.....	50
Figure 5.1 – DC polarization model	52
Figure 5.2 – Tafel plot (from [29])	53
Figure 5.3 – LSP application arrangement	56

Figure 5.4 – DC corrosion test sample.....	58
Figure 5.5 – DC polarization corrosion test setup	58
Figure 5.6 – Immersion test samples	63
Figure 6.1 – DC polarization corrosion current vs. potential	64
Figure 6.2 – DC polarization corrosion rates.....	65
Figure 6.3 – In-plane compressive stress vs. corrosion rate	66
Figure 6.4 – Immersion test weight loss measurements	67

List of Tables

Table 1.1 – Orthopedic material mechanical properties compared to bone (from [5, 8, 9])	5
Table 2.1 – AZ91D Chemical Composition (from [25])	15
Table 2.2 – AZ91D Material Properties (from [25])	16
Table 2.3 – LXR D Parameters.....	18
Table 2.4 – Vickers hardness comparisons.....	22
Table 2.5 – LSP trial 1 spot data.....	24
Table 2.6 – Vickers hardness of AZ91D before and after LSP	32
Table 3.1 – Model calibration specimen LSP parameters	38
Table 4.1 – AZ91 material properties	45
Table 4.2 – Initial reference	45
Table 4.3 – Validated Johnson-Cook parameters for Mg Alloy AZ91D.....	47

Chapter 1: Introduction

1.1 General Background

Biodegradable implants have become a topic of interest for the treatment of bone fractures and other bone conditions that require stabilization for healing. Biodegradable implants are used to heal bones while gradually dissolving and eventually becoming absorbed by the human body. Weiler et al. defines a biodegradable material as materials that show disintegration after implantation and subsequent complete excretion [1].

Most biodegradable materials currently being used are made of different types of polymers. Although these polymers have light weights and low densities, they do not have sufficient mechanical properties to support the bone while it heals [2, 3]. Another common solution for a bone fracture is to insert a non-degrading metallic implant over the fractured area to support the bone as it heals. Current available metallic implants include titanium, stainless steel, or cobalt-chromium alloys. These alloys have excellent corrosion resistance and very high strengths. However, these metallic implants have some disadvantages, including the need for a second surgical procedure for implant removal, revision procedures resulting from complications with the implant, and a problem known as stress shielding which can cause damaging effects to the healing process of the bone [2, 4]. Stress shielding is caused by a bone becoming shielded by an implant from carrying a load. The shielding occurs as a result of the implant removing normal stress from the bone, creating a reduction in bone density as it heals [2, 4].

Magnesium and magnesium alloy implants have many advantages over currently available biomaterials that make them a subject of interest in the medical industry. Magnesium is a light weight material, with a mass density much lower than the metallic implants described above. Magnesium and its alloys also obtain a relatively low elastic modulus compared to

current metallic implants. Its elastic modulus is much closer to that of the cortical bone, which makes magnesium implants ideal for avoiding stress shielding. Magnesium also has great biocompatibility as it is an essential element to the human body [5].

The main concern with magnesium and its alloys pertaining to their use as biodegradable implants is the corrosion behavior. Magnesium tends to corrode at rapid rates when immersed in body fluids. The rapid rates of corrosion create by-products such as hydrogen gas and hydroxides that are not ideal for the body to absorb [2]. The challenge with magnesium implants is the ability to control the corrosion rates in order reduce the harmful by-products created during rapid rates of corrosion.

Biodegradable implants are also subjected to different loading conditions while immersed in body fluids. This can lead to another problem relating to the rapid corrosion rates of magnesium known as Stress Corrosion Cracking (SCC). Stress Corrosion Cracking occurs when a material exposed to a corrosive environment fails or cracks under tensile stresses. Since biodegradable implants are meant to eventually completely degrade and become absorbed by the body, measures must be taken to ensure that the implant allows sufficient time for the bone to heal before failing. Controlling the SCC of magnesium is another challenge to overcome when implementing the use of magnesium alloys as biodegradable implants.

Laser Shock Peening (LSP), also referred to as Laser Shock Processing, is a material process in which compressive residual stresses are imparted on a material through the use of a high pulse energy laser. LSP is most commonly used to improve the fatigue life of metallic materials. The high compressive residual stresses that materials obtain from LSP are known to improve crack formation due to cyclic loading. However, new studies have been emerging

studying the effects of LSP on corrosion rates and Stress Corrosion Cracking of different materials.

The ability to control the corrosion rate of magnesium has been considered in many fashions. Corrosion rates can be controlled through alloying metals, surface coatings, and surface roughness treatments. A relatively new topic of interest is controlling corrosion rates by imparting compressive residual stresses on the surface of a material [2, 6, 7]. The effects of LSP on corrosion of magnesium has become very popular because the corrosion characteristics can be improved without the addition of different coatings and alloying elements that may not have great biocompatibility. This study explores the effects of Laser Shock Peening on the corrosion rates of magnesium.

1.2 Literature Review

1.2.1 Stress Shielding

When using biomedical implants to support hard tissue (i.e. bone), the materials must be designed to minimize the effects of stress shielding. Implants are typically used to support a bone while allowing it to heal. According to Wolff's law, the implant must be capable of maintaining a stress level in the bone as close as possible to the state of stress it experienced prior to fracture in order for the bone to heal properly [8]. For an implant that is oriented parallel to the direction of the load, the implant will take on a portion of that load. This causes a reduction in the load and, in-turn, stress that is applied to the bone. One way to reduce the effects of stress shielding by an implant is to create a good bond between the bone and implant. If the materials are well bonded, then the bone will experience the same deformation as the implant, which would create similar strain conditions [8]. The stress condition that the bone will

experience under a load that is parallel to the loading direction can be described with the equations (1.1.1) and (1.1.2).

Stress prior to implant:

$$\sigma_{bone} = \frac{E_{bone}P}{E_{bone}A_{bone}} = \frac{P}{A_{bone}} \quad (1.1.1) [8]$$

Stress with implant:

$$\sigma_{bone} = \frac{E_{bone}P}{E_{bone}A_{bone} + E_{implant}A_{implant}} \quad (1.1.2) [8]$$

The equations show that the reduction in stress that the bone will experience with the implant depends on the area and the modulus of elasticity of the implant. While the area of the implants is not necessarily material dependent, the modulus of elasticity is [8]. So a material with a higher modulus of elasticity will reduce or shield the bone from its normal stress conditions that it would experience without the implant.

In order to minimize the effects of stress shielding, while still maintaining sufficient strength to support the bone in the healing phase, a material must be selected that has an elastic modulus as close as possible to that of the human bone. It is also important to consider a lightweight material with other mechanical characteristics that match that of bone [5, 8]. *Table 1.1* shows some mechanical properties current metallic and polymer orthopedic implants compared to bone.

Material	Elastic Modulus (GPa)	Density (g/cm ³)	Yield Strength (MPa)	Tensile Strength (MPa)
Bone:				
Trabecular	0.005-0.15		0.5-50	7.6
Cortical	11-20	1.8-2.1	106-224	51-172
Metals:				
Magnesium	45	1.74-2.0	120-230	180-280
Stainless Steel	189-205	4.4-4.5	170-310	485
Co-Cr alloys	200-230	8.9-9.2	655	
Titanium alloys	110-117	4.4-4.5	758-1117	1000
Polymers:				
UHWPE	0.4-1.2	0.9-1	15.2-24.8	44
PMMA	1.4	1.2	90	45.5
PLA	0.6-4.0			11-72

Table 1.1 – Orthopedic material mechanical properties compared to bone (from [5, 8, 9])

The table shows that magnesium and magnesium alloys have properties that more closely match cortical bone in comparison to other materials. Other metallic implants have very high strengths and densities that would not make them favorable for use as orthopedic implants to cortical bone. While the polymer materials have densities similar to cortical bone, their strengths are much lower, which makes them favorable for use with trabecular bone rather than cortical bone [5, 8, 9].

1.2.2 Magnesium as Biodegradable Implants

Magnesium is an essential element to the human body as it contributes to metabolism and is naturally found in bone tissue [10]. The average person consumes 300-400 mg of magnesium each day [9-11]. This understanding has made magnesium implants a topic of interest in the medical industry for over 100 years, although little success has been made in the area.

1.2.3 Brief History

Magnesium alloys have been considered for use and surgical implants as early as 1907. A French surgeon, Lambotte, was the first to attempt to use magnesium implants when he tried

to use a pure Mg plate as an implant to secure a lower leg fracture [9, 10]. His attempt was unsuccessful due to the rapid corrosion rate of magnesium. The implant disintegrated after only 8 days and produced a large amount of gas beneath the skin [10, 12]. Other attempts were made to use Mg as orthopedic implants, but its rapid corrosion rates continued to create problems; not only in maintaining its structural integrity but also the formation of gas cavities due to rapid corrosion [12].

In 1944, Troitskii and Tsitrin developed a magnesium-cadmium alloy implant with a reduced corrosion rate and maintaining its mechanical integrity from 6-8 weeks after insertion, and complete resorption in 10-12 months. The implant was shown to simulate the bone healing process without producing any toxic effects [10]. In 1945, Znamenski reported the use of a magnesium-aluminum alloy to treat gunshot wounds. In the two cases reported, fractures were shown to be completely fused with no detection of the implant after 6 weeks [10].

These early uses of magnesium implants have shown that the implants are capable of successfully healing bones without creating toxic gases if the corrosion can be properly controlled. However pure magnesium and simpler alloys still corrode too rapidly to be used as implants. It is desirable for the biodegradable implant to maintain its mechanical integrity for at least at 12 weeks [10]. However the time for the implant to maintain its mechanical integrity may vary due to the type, nature, and severity of the fracture. For these reasons, it has become desirable to be able to control the corrosion rate of biodegradable implants.

1.2.4 Corrosion Resistance of Magnesium and Magnesium Alloys

As described, magnesium has many obvious advantages that make it favorable for use as a biodegradable material, but the concerns involve its corrosion resistance and the toxicity levels

it gives off during corrosion. Equation (1.2.1) shows the corrosion reaction of pure magnesium at its corrosion potential.



The normal product (Mg^{2+}) can easily be absorbed by the human body [9, 11, 12]. However, rapid corrosion rates during degradation cause hydrogen evolution and alkalization of solution [11, 12]. The H_2 and OH^- bubbles can accumulate in gas pockets around the implant, which can prevent the bone from healing because this can cause a separation of tissues and tissue layers [11]. In serious cases, if the hydrogen gas bubbles are large and get caught in the blood circulating system, they can block blood flow and possibly result in the death of the patient [11]. Alkalization occurs when high concentration hydrogen ions form in the body, causing the pH level to rise. Song et al. proved that a 1cm x 1cm x 1cm sample of pure magnesium can cause an increase in pH value of Hank solution from 7 to 10 over a 15 hour period [13]. It is not ideal for the pH value in the body to be higher than 7.8. This increase in pH level occurs due to the rapid corrosion rate of Mg creating hydrogen ions. The body is capable of adjusting its pH level on its own, but not when it is changing at such rapid rates. If the corrosion rate can be decreased, the body will adjust the pH level back to around 7.8 without causing any harm [11, 13].

1.2.5 Stress Corrosion Cracking (SCC) of Magnesium

Not only will biodegradable magnesium implants be subject to corrosive environments, but will also experience different loading conditions in that environment. A material under tensile loads in a corrosive environment can develop cracks or begin to fail earlier than it would in a non-corrosive environment. This phenomenon is known as Stress Corrosion Cracking (SCC). Studies have shown that magnesium alloys typically experience Transgranular Stress Corrosion Cracking (TGSCC) due to Hydrogen Embrittlement (HE). HE occurs when cracks

form through or across the grains of the material due cathodic reaction between the hydrogen ions formed during Mg corrosion [14, 15]. It is very important to be able to eliminate the formation of SCC of biodegradable implants in order for the bone to heal properly.

1.2.6 Applications and Potential Benefits of LSP on Magnesium Alloys

Laser Shock Peening (LSP) is a process that uses a high pulse laser to create a shock wave which leaves compressive residual stresses on a material that can be beneficial in many ways. Many applications of LSP relate to the increased compressive residual stress through the depth of a material and the ability to control the fatigue strength, fatigue life, hardness, and development of surface cracks [16]. LSP is most commonly used in the aerospace industry to treat turbine blades, gears, shafts and other rotor components that may develop cracks or be damaged by the intake of foreign objects [16]. In the late 1990's, General Electric Aircraft Engines began using LSP to treat the leading edge of turbine blades on military aircrafts to protect them for foreign object damage [16].

More recent studies have been conducted investigating the effects of LSP on corrosion rates and stress corrosion cracking of different materials. Fabbro et al. was one of the first to study the effects of LSP on pitting corrosion resistance of stainless steels. It was discovered that LSP can improve the pitting corrosion behavior of 316L stainless steel due to the high compressive residual stresses and work hardening created during LSP [7]. It has been documented that the grain refinement of a material which results from LSP along with the compressive residual stresses can have beneficial effects on corrosion resistance of materials, specifically the pitting corrosion, which can lead to improvements in SCC as well [17]. Newer studies are investigating if LSP can improve or eliminate SCC in different materials, mostly in the nuclear and power industries.

The benefits described above show that LSP would be an ideal material process to help improve surface corrosion, stress corrosion cracking, as well as the fatigue life of magnesium alloys to be used as medical implants. Little research has been done regarding LSP on magnesium alloys. Huang et al. has conducted an experimental study performing LSP on magnesium alloy AZ31B and was able to achieve surface compressive residual stresses on the order of 200 MPa, while the grain sizes were refined from about 7 μm to about 4 μm [18]. Zhang et al. also conducted a study investigating the effects of LSP on the stress corrosion cracking susceptibility of magnesium alloy AZ31B, in which a surface compressive residual stress of about 250 MPa was achieved and the SCC crack depth was reduced from a length greater than 0.4 mm without LSP to about 0.2 mm with LSP [6]. Although a few studies have been performed relating to LSP on Mg alloys, there is still much to explore on this topic, which this thesis will investigate.

1.3 Laser Shock Peening

1.3.1 Background

Laser Shock Peening (LSP) is a relatively new material process that is used to impart high levels of compressive residual stresses on a material through the high energy pulse of a laser beam. The theory of LSP originated in the 1960's when R.M. White began studying elastic wave produced by electron beam impacts on solids under a vacuum [19]. Later studies focused on the origin of the elastic wave generated by electron beams on solids under a vacuum, in which this phenomenon was referred to as thermal impact [20]. The term thermal impact was eventually attributed to the theory known as laser ablation. Laser ablation occurs when a thin layer of material is vaporized as a result of intense radiation created by a laser beam [20]. In 1969, Anderholm discovered that the use of a transparent material and thin film absorber over the material can generate much higher amplitudes of the elastic stress wave and increase the

duration of the pressure pulse created in the process [21]. The transparent material is used to impede the expansion of the vaporized absorber [21]. This increase in amplitude is capable of leaving plastic deformation in the material that can modify the microstructure and mechanical properties of the material [22]. Research on LSP continued through the 1980's and 1990's as a number of patents were issued within the aerospace and automotive industries and the process continued to improve.

1.3.2 Physical Process

During the Laser Shock Peening process, residual stresses are imparted on a material through a high energy laser with power densities up to 10 GW/cm^2 over pulse durations of 1-50 nanoseconds. *Figure 1.1* represents the physical process of LSP.

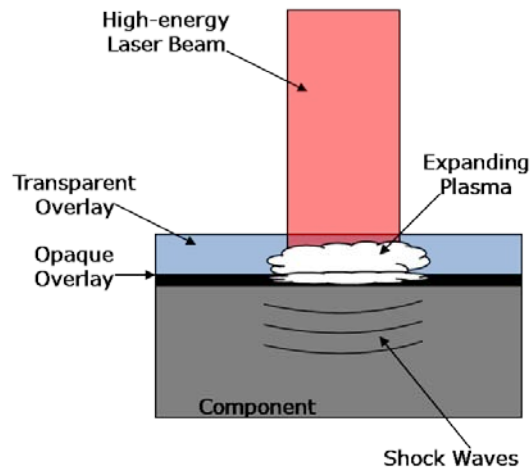


Figure 1.1 – LSP configuration (from [22])

The LSP process typically consists of the material being treated, a sacrificial, or opaque, overlay, and a transparent overlay. The sacrificial overlay is usually a layer of black tape or paint with a known thickness and the transparent overlay is a thin layer of water flowing at a constant stream. When the high-energy laser pulse is applied, it passes through the transparent overlay and irradiates the opaque overlay. The laser then vaporizes part of the opaque overlay and heats

up. The heat ionizes the vapor and creates a high-energy plasma cloud, which expands rapidly. Since the overlays prevent the plasma cloud from interacting with the surface of the metal (which could damage the surface), a high pressure pulse is exerted on the material. The transparent and opaque overlays are used to make LSP purely a mechanical process. The pressure pulse creates a shock wave that propagates through the material, which creates the plastic deformation and changes in microstructure. The plastic deformation of the material typically results in compressive residual stresses surrounded by a region of tensile stresses. It is the depth of the compressive residual stress that makes LSP a unique surface treatment process, as opposed to conventional shot peening [22]. The compressive stresses travel up to 400-600 μm in depth, which makes LSP an ideal material processing treatment to improve fatigue life, corrosion, and stress corrosion cracking [22]. LSP also creates some strain hardening and improves the materials surface hardness.

1.3.3 Temporal Shape

As described, LSP creates a high pressure pulse on which generates a shock wave throughout the material that creates plastic deformation and residual stresses. The pressure pulse that is created by LSP can be analyzed through what is known as the power density of the laser. The power density is based on the energy generated by the laser, pulse duration, and the surface area which the laser is acting on. For the purposes of this study, the power density for LSP is referred to in units of GW/cm^2 and is calculated with the following equation:

$$PD (\text{GW}/\text{cm}^2) = \frac{\text{Laser Energy (J)}}{\text{Surface Area (cm}^2\text{)*Pulse Width (ns)}} \quad (1.3.1)$$

The power density is only part of the model. In order to determine the intensity of the pressure load acting on the material, the pulse shape must be known. There are typically two

types of pulse shapes that are possible for LSP. The most commonly used pulse is the Gaussian pulse. The Gaussian pulse is a function of peak time, peak duration (FWHM), and maximum intensity, as shown in equation (1.3.2).

$$I(t) = Ae^{-\frac{(t-b)^2}{2c^2}} \tag{1.3.2} [22]$$

Where I is the temporal intensity, A is the maximum intensity, b is the peak time, and c is a function of the full width half max (FWHM) as shown in equation (1.3.3).

$$FWHM = 2\sqrt{2\ln(2)} \cdot c \tag{1.3.3} [22]$$

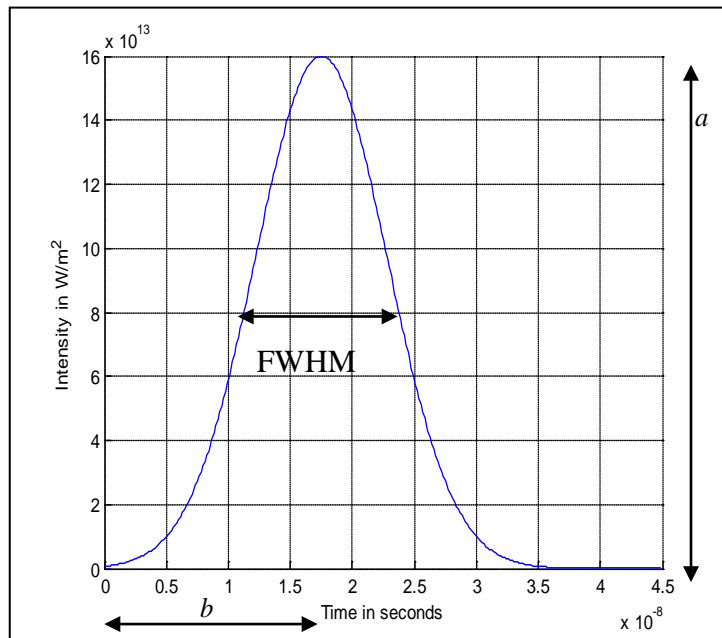


Figure 1.2 – Gaussian peak (from [22])

Although the Gaussian peak was common for many years, it has been shown that it does not give the best results [23]. Devaux et. al. has proved that a Short Rise Time (SRT) peak can be more effective in achieving higher peak pressure. SRT peaks have been shown to increase the peak pressure 4-5 times that of a typical Gaussian temporal profile [23]. The SRT peak can decrease the effects of dielectric breakdown of the laser and can generate more

effective power densities and higher peak pressures [23]. Higher peak pressures generated from SRT peaks are capable of increasing the depth of the residual stress.

The SRT profile can be represented with two parts: a cosine profile for the SRT region and the Gaussian profile for the remaining region and is represented by equation (1.3.4). *Figure 1.3* shows a typical SRT peak profile.

$$I(t) = \begin{cases} \frac{A}{2} \left(1 - \cos \frac{\pi \cdot t}{\text{Rise Time}} \right), & t \leq \text{Rise Time} \\ A \cdot \exp \left(-(t - \text{Rise Time}) \left(\frac{t - \text{Rise Time}}{2 \cdot \frac{c^2}{2.355}} \right) \right), & t > \text{Rise Time} \end{cases} \quad (1.3.4) [22]$$

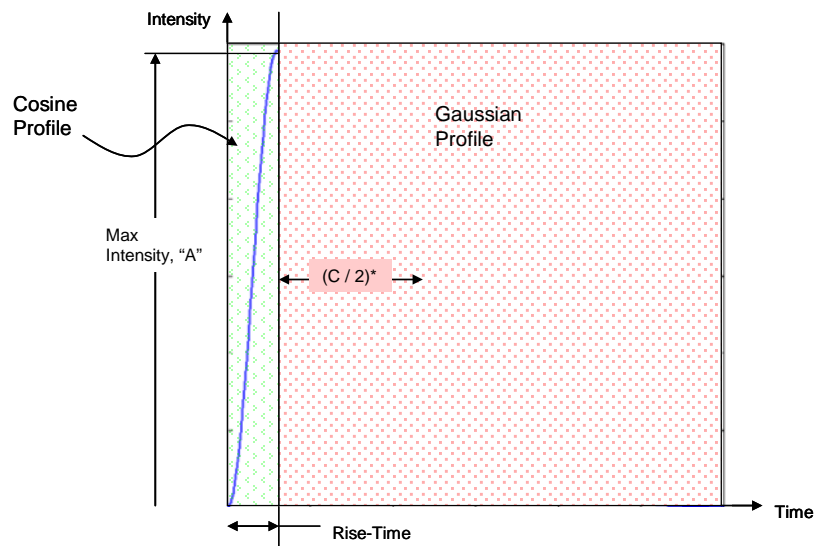


Figure 1.3 – Short rise time peak profile (from [22])

The SRT peak is used for all LSP studies performed in this paper. For each individual shot, the rise time, pulse width, and laser energy are recorded from the laser system to determine the pressure pulse. The FWHM of the peak is necessary for determining power density and is commonly referred to as “pulse width.”

1.4 Objective

The objective of this thesis is to investigate the effects of residual stresses imparted through Laser Shock Peening on the corrosion characteristics of Mg alloy AZ91D. Material characterization through microstructure analysis, hardness tests, residual stress measurements, and heat treatment will be performed prior to LSP. Once characterization data is obtained, an experimental residual stress study will be performed to determine the best method to achieve compressive residual stresses on the material. In order to better observe the residual stress effects of LSP on the material based on material characterization data, Finite Element Analysis will be performed using LS-DYNA to validate and optimize the LSP method. Once the LSP parameters are optimized, experimental procedures will be conducted to investigate the effects of compressive residual stress on the corrosion resistance of Mg alloy AZ91D. The goal of this thesis is to draw conclusions between to the effects of LSP on the material characteristics and the corrosion resistance of AZ91D.

Chapter 2: Material Characterization

For many magnesium alloys, aluminum is commonly used as the alloying element because of its low price, availability, low density and corrosion and strength properties [24]. The material under investigation in this thesis is magnesium alloy AZ91, which is a magnesium-aluminum-zinc alloy. AZ91 is one of the more commonly used magnesium alloys because of its high strength at room temperature, great castability, and corrosion resistance [24]. The AZ stands for Aluminum-Zinc and the following numbers represent the percent of aluminum and zinc in the alloy, respectively. The material used for all experiments in this study is AZ91D, which is a high purity alloy and has the following chemical composition and material properties provided by the manufacturer:

AZ91 Chemical Composition	
Aluminum	8.3-9.7%
Manganese	0.15% min.
Zinc	0.35-1.0%
Silicon	0.10% max
Iron	0.005% max.
Copper	0.030% max.
Nickel	0.002% max
Other	0.02% max.
Magnesium	Balance

Table 2.1 – AZ91D Chemical Composition (from [25])

AZ91 Material Properties	
Young's Modulus	45 GPa
Poisson's Ratio	0.35
Tensile Strength	230 MPa
Yield Strength	160 MPa
Specific Heat	1.05 kJ/kg-k
Density at 20°C	1.81 g/cm ³
Melting Temp.	700°C

Table 2.2 – AZ91D Material Properties (from [25])

2.1 Microstructure Analysis

Magnesium-aluminum alloys are characterized as a solid solution of aluminum in magnesium with a hexagonal close packed (HCP) microstructure. AZ91D consists of an α -phase (Mg), a γ -phase, sometimes referred to as the β -phase, ($Mg_{17}Al_{12}$), and a $\alpha+\gamma$ eutectic phase [24]. The eutectic phase can be fully or partially divorced, depending on the solidification process and the aluminum content. Non-equilibrium solidification will cause the γ -phase to form large crystals, depleted in alloying elements, and will push the aluminum mixture into the interdendritic spaces [24]. This can be seen in the phase diagram shown in *Figure 2.1*.

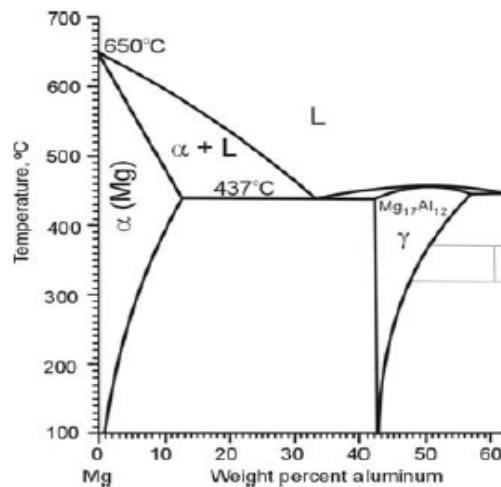


Figure 2.1 – AZ91 phase diagram (from [24])

Microstructure analysis was performed on the AZ91D samples as-received from the manufacturer prior to experimental work. As-received samples were finely polished on 1200-grit silicon carbide polishing sheet and etched using a mixture of ethanol (100 mL), water (20 mL), acetic acid (1 mL), and picric acid (5 mg).

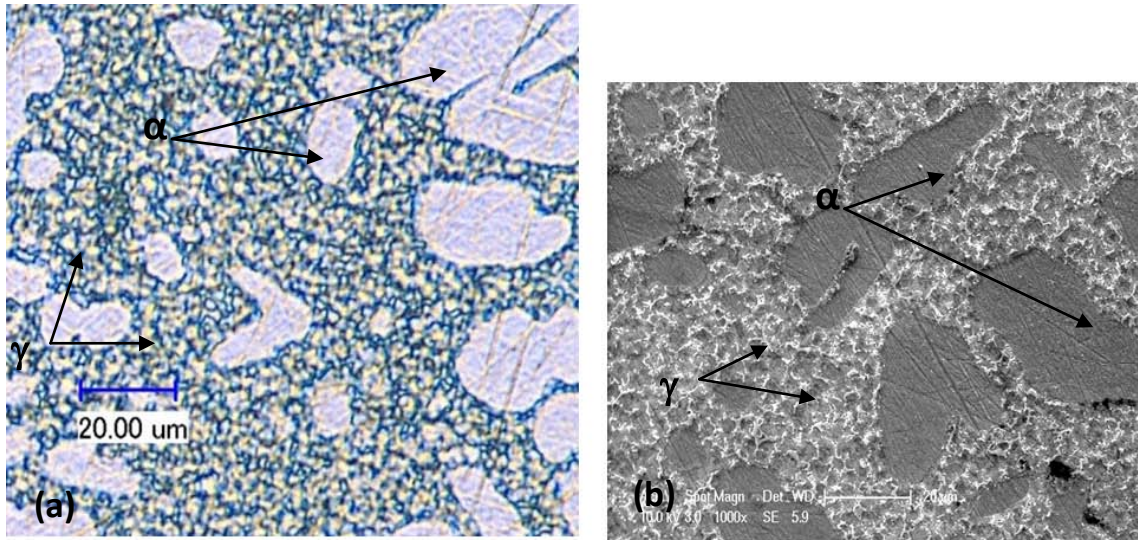


Figure 2.2 – AZ91D microstructure as-received polished and etched (a) optical (b) SEM

Figure 2.2 shows the microstructure of as-received AZ91D after polishing and etching. These images show precipitates of the γ -phase in the α -phase. However, no obvious grains or grain boundaries can be seen. This is likely due to the casting and solidification process of the material along with the high aluminum content of AZ91.

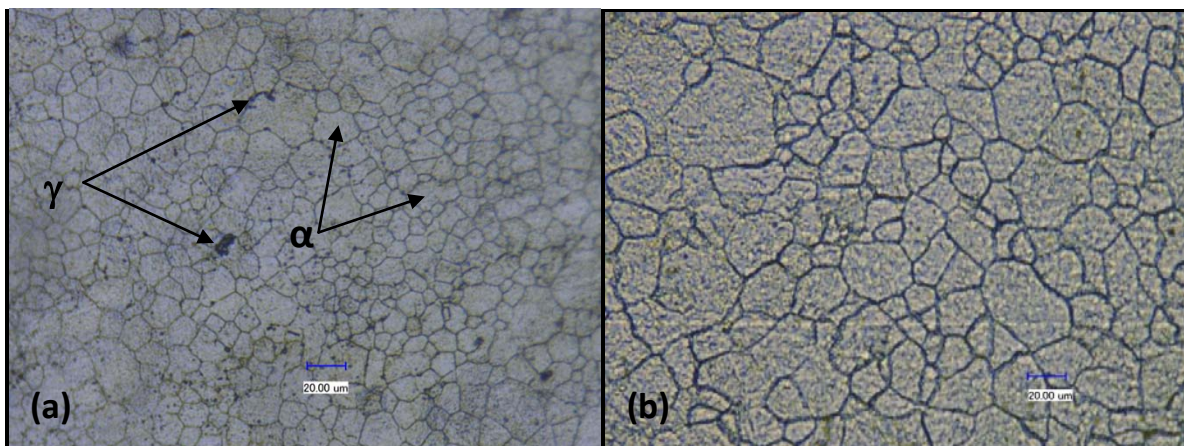


Figure 2.3 – As-received polished and etched (a) AZ31 (b) pure magnesium

Figure 2.3 shows the microstructure of as-received Mg-Al alloy AZ31 (~3% Al, 1% Zn) and the pure magnesium. Each material was polished and etched with the same process described above. Each of these images reveals an obvious HCP microstructure. While AZ31

does have some precipitates of the γ -phase near the grain boundaries, it is not nearly as prevalent as in AZ91. Pure Mg only contains an α -phase (Mg) and has a slightly larger average grain size than AZ31. This could be due to casting, solidification, or any prior heat treatment performed on the materials.

2.2 X-Ray Diffraction & Residual Stress Measurements

X-ray diffraction (XRD) is a process commonly used to evaluate the microstructure of crystalline solids. When X-rays interact with a planar phase where the atoms along the plane are aligned, a diffraction pattern can be observed along the detector angle, also known as the Bragg angle. This pattern is typically observed as a peak, or spike in intensity at the diffraction angle. XRD is not only used for observing the microstructure orientation of a material, but also to detect the residual stress. Residual stress is determined based on a predefined plane, diffraction angle of the plane, and set of elastic constants for the particular material. A well defined XRD pattern is essential to analyzing the residual stress of a material.

In this study, all residual stresses (RS) are measured using the Proto™ LXR Stress Measurement System. All measurements for magnesium and magnesium alloys were measured using the following Proto™ recommended parameters:

X-ray Tube	Cr_k-alpha
Wavelength	2.291Å
Diffraction Plane	104
Bragg Angle	152°
$\frac{1}{2}S2$	27.83×10^{-6}
-S1	6.09×10^{-6}
$(E/(1+\nu))_{eff}$	35,932.45
$(E/\nu)_{eff}$	164,203.61

Table 2.3 – LXR Parameters

When residual stresses are measured on an as-received sample of AZ91D using the parameters defined in *Table 2.3*, no definite peak can be observed, as shown in *Figure 2.4 (b)*. This is likely due to the high aluminum content in AZ91 compared to other Mg-Al alloys, such as AZ31, as well as the casting and solidification process. The XRD peak for as-received AZ31B can be shown in *Figure 2.4 (a)*. *Figure 2.2* shows that there is a high content of precipitates of the γ -phase ($\text{Mg}_{17}\text{Al}_{12}$) in the α -phase (Mg), which is likely causing the absence of a defined XRD peak in that region. The phase diagram in *Figure 2.1* indicates that for the percentage of aluminum in AZ91 (~9%), heating the material to $\sim 420^\circ\text{C}$ will cause total dissolution of the primary γ -phase or the eutectic $\alpha+\gamma$ phase and will homogenize the aluminum throughout the matrix [24]. Braszczyńska-Malik indicates that the optimum heat-treatment process for AZ91 to allow for this to occur is to anneal the sample at for a minimum of 24 hours at a temperature of 420°C [24]. Annealing was performed as described on the AZ91D samples. After annealing, an obvious grain structure and XRD peak was able to be observed as shown in *Figure 2.4 (c)*. An increase in the peak intensity allows for accurate residual stress measurements, which are important to this study regarding the effects of LSP on AZ91.

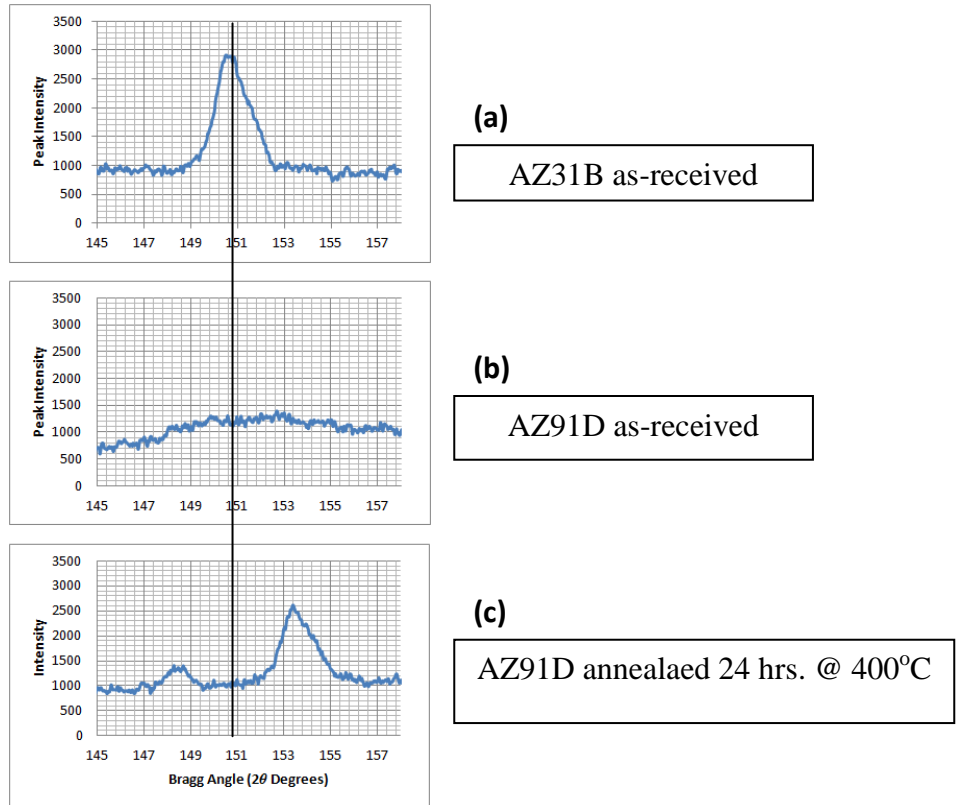


Figure 2.4 – LXR D peak comparisons between (a) AZ31B (b) as-recieved AZ91D, and (c) AZ91D after annealing for 24 hrs. at 400°C

A full XRD scan was also performed on AZ91D before and after annealing to observe the phase changes over a larger range. *Figure 2.5* shows that annealing at 400°C for 24 hours causes an increase in the peak intensity of the α -phase and a decrease in intensity of the γ -phase.

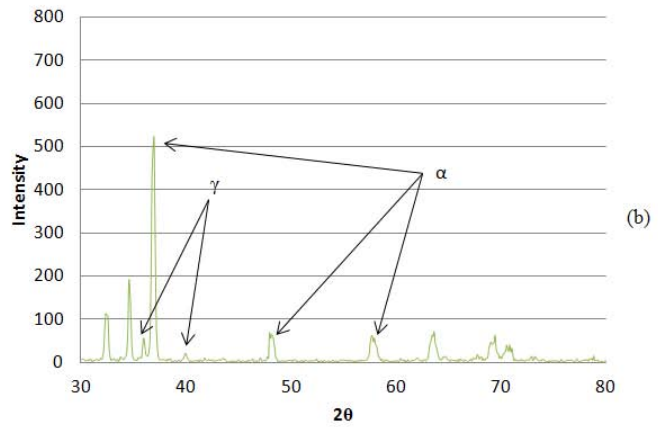
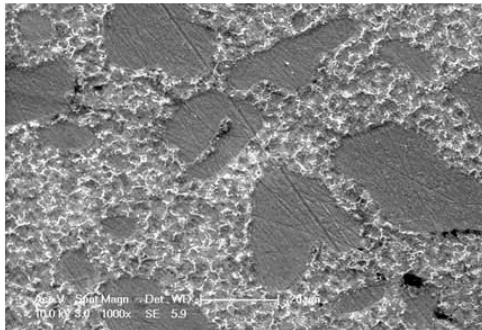
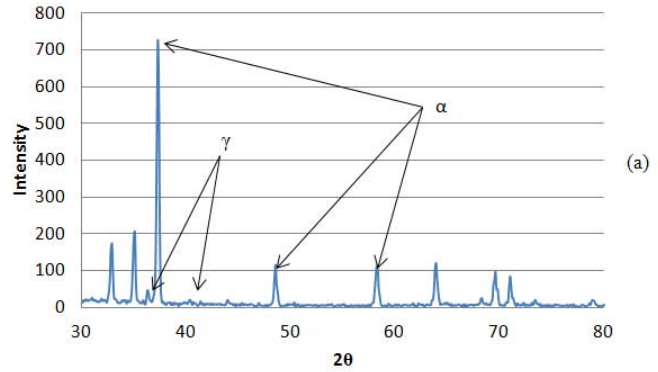
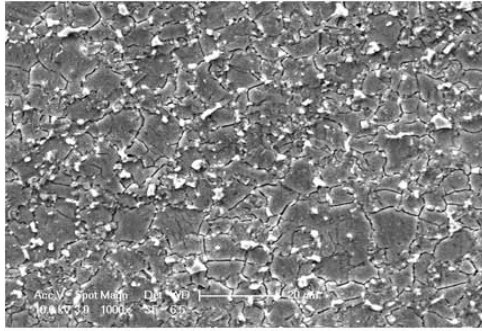


Figure 2.5 – XRD patterns (a) annealed and (b) as-received

The optical and SEM images shown in *Figure 2.6* reveals that the γ -phase did not completely dissolve in the matrix, but it has been depleted, and pushed towards the grain boundaries. All samples used for experimental purposes were annealed to these conditions to obtain accurate residual stress measurements.

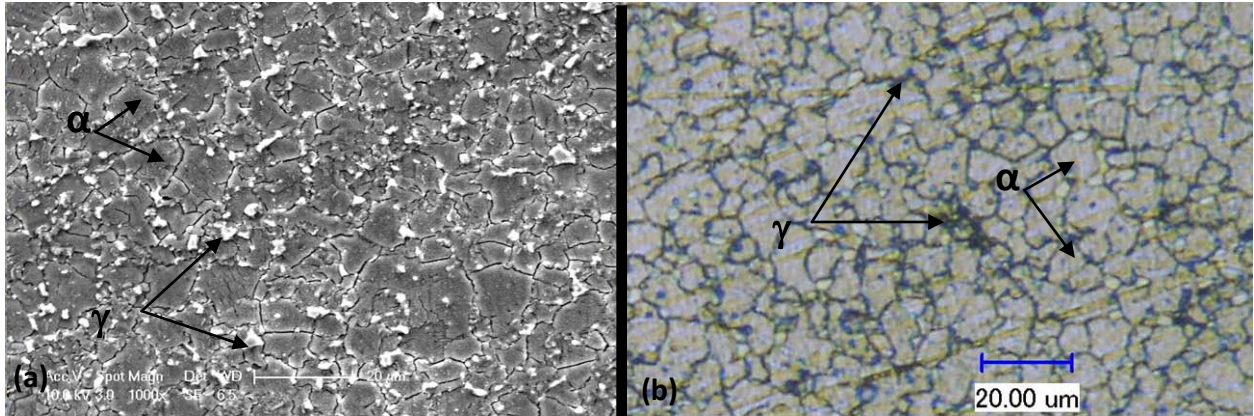


Figure 2.6 – AZ91D after annealing for 24 hours at 400°C (a) SEM, (b) optical

2.3 Hardness

Magnesium is a much softer material than most metals that have had been used for LSP applications. The hardness of the material is a very important characteristic for the material to maintain high levels of residual stress. The hardness of the material can have effects on the dampening characteristics of the shock wave created from LSP, as well as the flow of the stress. The Vickers hardness of AZ91D before and after annealing was measured using micro-indentation and is shown in *Table 2.4*.

Material	Vickers Hardness
AZ91D (as-cast)	105.34 HV
AZ91D (Annealed)	84.195 HV
Ti-6Al-4V	300-350 HV
Co-Cr alloys	410-545 HV

Table 2.4 – Vickers hardness comparisons

Table 2.4 shows that the Vickers hardness for AZ91D is much lower than the metals that are currently used as medical implants. There is also about a 20% decrease in hardness after annealing.

2.4 Residual Stress Characterization

A series of LSP trials were performed on different sets of AZ91D coupons in order to determine the best method of LSP to obtain high levels of compressive residual stress. Since the objective of this study is to relate the effects of compressive residual stresses created from LSP to the corrosion rate of AZ91D, it is necessary to achieve high levels of compressive residual stress on the surface of the material. In a corrosion test, the peened surface will be exposed to the corrosive fluid, so the surface stress of the material is the most important. However, the depth of the stress through the thickness of the material will also be important in relating to stress corrosion cracking and fatigue analysis, as well as developing an accurate finite element model. Once an optimum level of residual stress is reached on the surface, a depth profile of the stress through the thickness can be obtained.

For all trials, samples were covered with black tape to act as the opaque overlay and water was run over them to act as the transparent overlay as shown in *Figure 1.1*. The laser energy and pulse width were recorded from each shot. In-plane stress was measured with the Proto™ LXR D Stress Measurement System using the material parameters listed in *Table 2.1*.

2.4.1 LSP Trial 1

Single sided LSP was initially performed on a single 12mm x 100mm x 3.3mm coupon of magnesium alloy AZ91D, as-received from the manufacturer, with eight (8) single shots of approximately a 2mm diameter at four (4) different energy levels (2J, 4J, 6J, and 8J), along a 2J, 4mm x 4mm patch, a 4J, 4mm x 4mm patch, and a 2J, 10mm x 10mm patch with a 50% overlay for each spot.

After LSP was performed, the dimple depths and dimple diameters for each single shot were obtained using a Veeco™ Profilometer. Next, the surface stresses were measured using a Proto™ LXR Stress Measurement System. The following results were obtained.

Spot ID	Power Density (GW/cm ²)	Residual Stress (MPa)	Error
As-received-1	0	-43.2	±16.2
As-received-2	0	-48.89	±19.4
LSP1-2J-1	2.39	-26.91	±17.8
LSP1-4J-1	3.13	6.52	±13.8
LSP1-4J-2	3.61	-3.18	±21.5
LSP1-6J-1	4.81	16.55	±16.9
LSP1-6J-2	4.44	23.16	±11.2
LSP1-8J-1	5.42	60.42	±18.7
LSP1-8J-2	5.85	20.38	±17.5

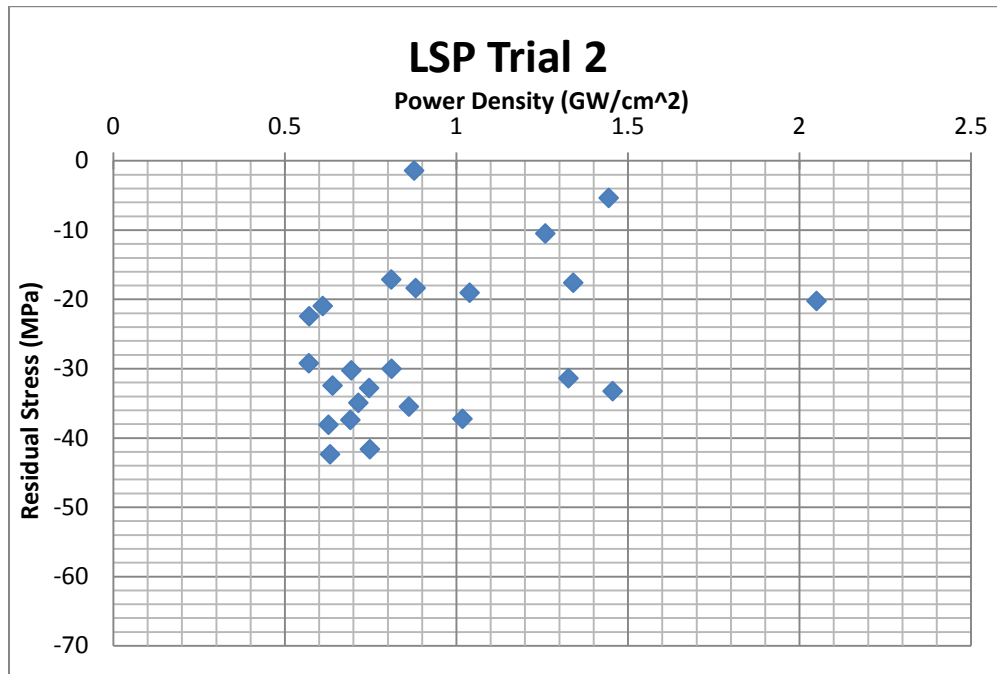
Table 2.5 – LSP trial 1 spot data

The data in *Table 2.5* indicated that the surface stress was increasing into the tensile region with higher power densities. It can also be observed the residual stress measurement errors are relatively high due to the inadequate XRD peak in the as-received samples. The measurement errors are defined by a Gaussian curve fit to the measured XRD peak. Therefore, if the measured XRD peak is not well defined, it will give a high error.

2.4.2 LSP Trial 2

After analyzing data from the initial trial, it was determined that the next set of LSP performed will use lower energy levels and larger spot diameters to decrease the power density in hopes that this will create some higher levels of compressive residual stress. This time, the samples were annealed at 400°C for 24 hours in order to achieve accurate residual stress measurements. After annealing, unpeened specimens were observed to have an initial residual stress of approximately 0.0 MPa ± 3.3 MPa.

The goal of the second set of LSP on AZ91D was to lower the power density. This was done by increasing the spot diameter from 2mm to approximately 4mm. Four 20mm x 100mm x 3.3mm coupons were prepared. Single sided LSP shots were performed at four different energy levels: 2J, 4J, 6J, and 8J (one energy level per coupon), with a minimum spacing of 20mm between spots to avoid interaction between shots. The following results were obtained from the second LSP trial.



In this case, the coupon was peened simultaneously from both sides, with each channel of the laser aligned so that the impact occurred at the same spot.

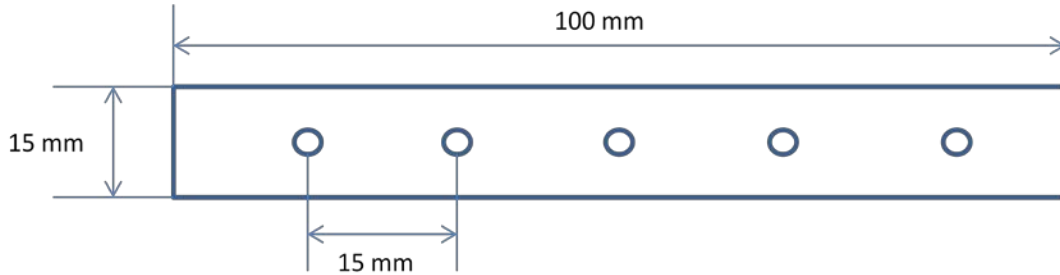


Figure 2.8 – 15mm x 100mm x 3.0mm coupon

LSP was performed on a coupon as shown in *Figure 2.8*. All samples were annealed at 400°C for 24 hours prior to peening. After annealing, unpeened specimens were observed to have an initial residual stress of approximately 0.0 MPa \pm 3.3 MPa. Each side of the coupon was labeled to the corresponding channel of the laser and the LSP parameters were recorded for each side. The results from this trial are shown in *Figure 2.9*.

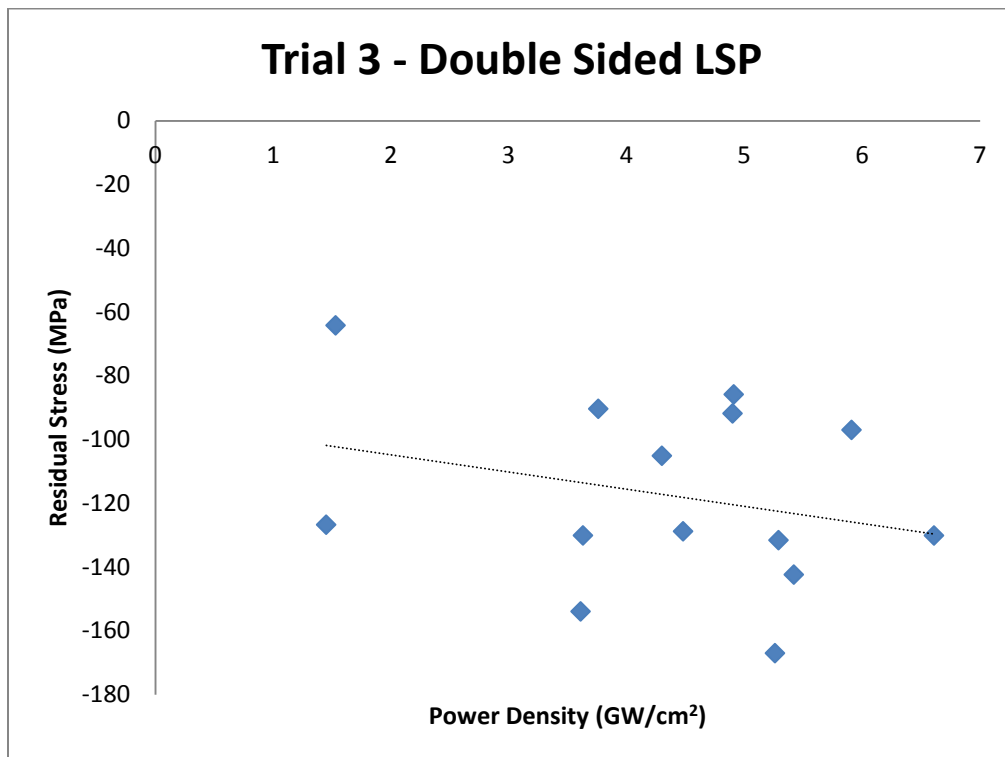


Figure 2.9 – LSP trial 3 results

As shown in *Figure 2.9*, double-sided LSP yields relatively high levels of compressive residual stress on the surface of the material. The stress values range from approximately -60 MPa to -170 MPa. While these values are not nearly as high as materials that are commonly used in LSP applications (Titanium, aluminum, steel, etc.), the stress is relatively high with respect to the initial yield stress of magnesium. There appears to be no distinct correlation between the measured surface residual stress and the power density from the laser. This is likely due to the inconsistency of the laser. Although the laser is peening each side simultaneously, the power density that is output from each channel of the laser was never the same. This can have some effect on the magnitude and speed of the shock wave traveling through the material and likely is causing the differences in the resulting surface stress.

2.5 LSP Characterization

Once acceptable levels of compressive residual stress were obtained for AZ91D, some material characterization was performed on peened samples to study the effects of LSP on the microstructure and mechanical properties.

2.5.1 Spatial Variation

The laser being used has been shown to have some spatial variation in the intensity profile. For most materials that have been experimented on, a spatial profile of the dimple shows some non-uniform distribution. One way to obtain the spatial profile of a dimple is through White Light Interferometry. This done using a Veeco™ Profilometer to scan the LSP dimples. This instrument can also be used to determine the spot diameter of the dimple. *Figure 2.10* shows spatial profiles of LSP performed on AZ91D.

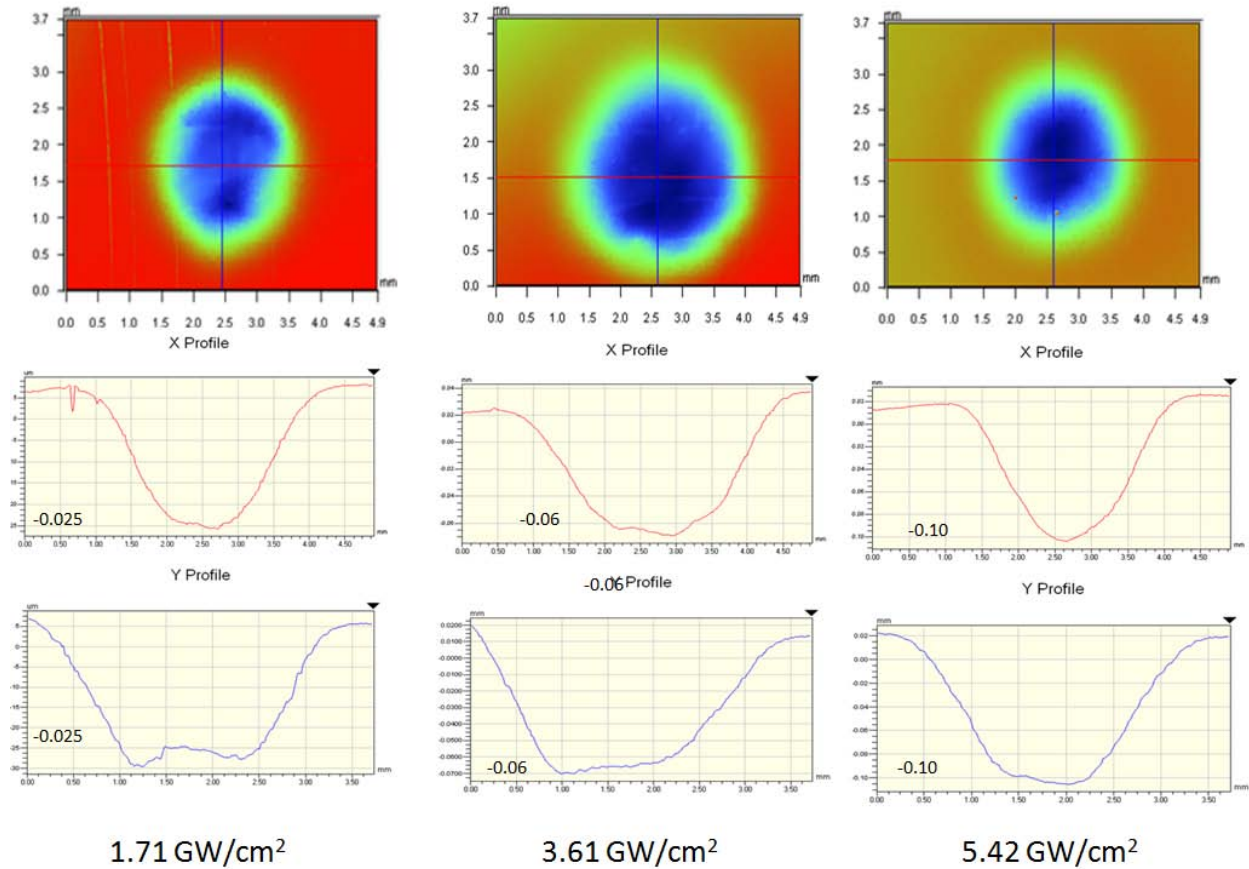


Figure 2.10 – Veeco spatial profiles

The spatial profiles shown in *Figure 2.10* all have relatively uniform profile shapes, with dimple depths that range from 25 μm to 100 μm over a good range of power densities. The uniform distribution and high dimple depths are likely due to the softness of magnesium in comparison to other materials that are commonly used in LSP applications. For harder materials (Ti64, steel, etc.), dimple depths usually lie in a range between 5 μm to 20 μm . From the data collected, it has been determined that a uniform spatial distribution will be assumed for all modeling and simulation work.

2.5.2 Stress Depth Profile

When performing LSP on a material, it is important to know the magnitude of compressive stress that is maintained through the thickness of the material. This is very

important for materials in which fatigue, tensile, or SCC are of interest in analyzing the effects of LSP. While this thesis is only focusing on surface corrosion, there are future plans of performing SCC and fatigue analyses on AZ91D.

Residual stress depth profiles were measured using a combination of electro-chemical polishing and LXRD measurements. Electro-chemical polishing was used to polish off layers of the surface using Struers™ AC2 solution, which is recommended for use with Mg-Al alloys. The thickness of the sample was measured and recorded in between each polishing sequence. The residual stress of the material was also measured and recorded in between each polishing sequence. A through-depth gradient correction, based on the chemical composition of the material, is required for an accurate depth profile. The Proto™ LXRD Stress Measurement System accounted for the gradient depth correction using a built-in function and chemical composition of AZ91D. The following stress-depth profiles were obtained.

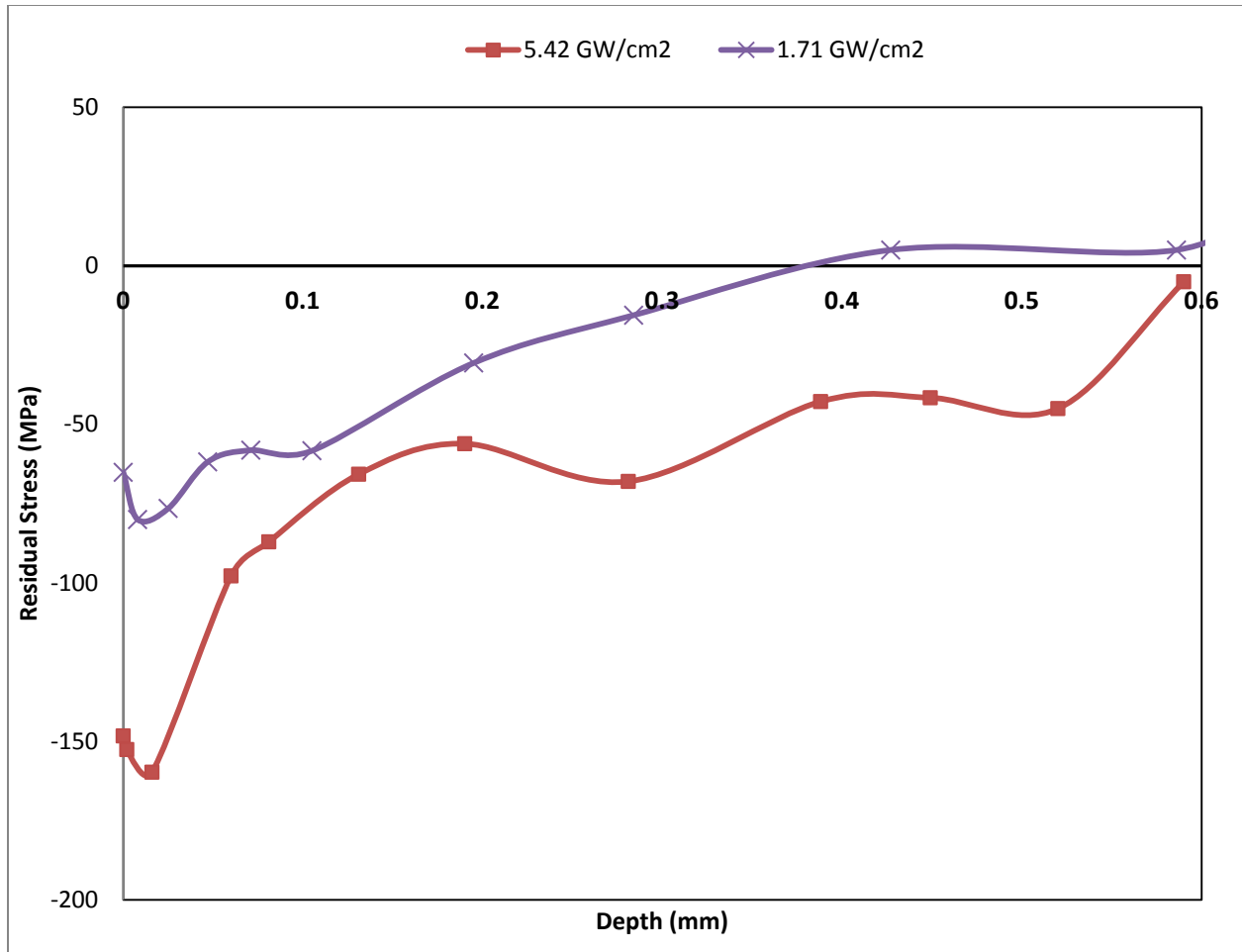


Figure 2.11 – Stress depth profiles

The stress depth profiles were selected to be performed on spots within the higher level of measured surface stress (-170 MPa) and lower RS (-60 MPa), so that a good range of stress levels can be captured. It can be observed that the residual stress initially decreases about 15 to 30 MPa within the first 15 μm and then slowly increases and eventually reaches a tensile region between 400 to 600 μm .

2.5.3 Microstructure after LSP

The microstructure of the peened samples was observed after LSP to document the changes in grain structure and grain size. However, optical and SEM images did not reveal any significant signs of microstructure changes due to poor image quality within the dimple. These

images are not included in this thesis. Future studies should include LSP patches and electron backscatter diffraction (EBSD) scans to obtain more accurate microstructure images.

A full XRD scan was performed analyze the effects of LSP on the lattice structure. *Figure 2.12* shows the XRD pattern of AZ91D before and after LSP. Although it is not clear from the picture shown, further analysis indicates that the high-angle peaks for the peened material are slightly larger than that of the unpeened material, indicating a slight shift to the right. These peak-shifts indicate compressive residual stresses which can likely be attributed to grain refinement that occurs from LSP as well as the effects of work hardening local strains on the surface of the material.

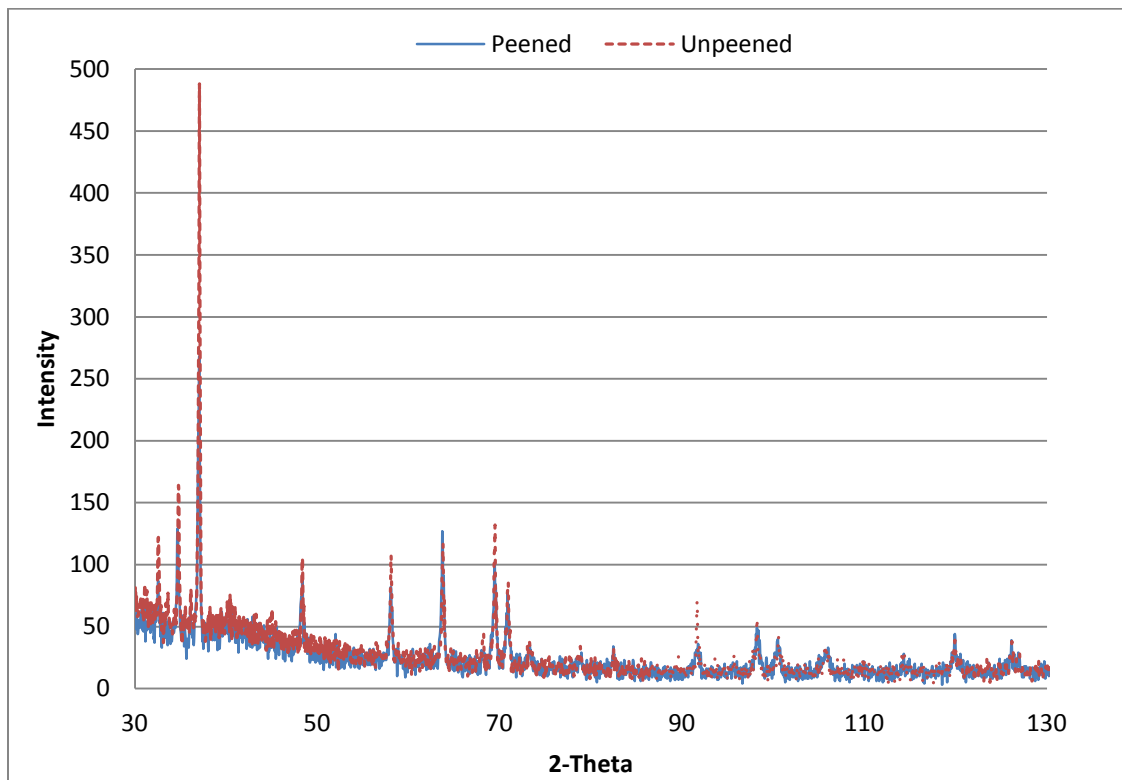


Figure 2.12 – XRD patterns of AZ91D before and after LSP

2.5.4 Hardness after LSP

Micro-indentation was performed on peened samples to check the Vickers hardness after LSP was performed on the coupons. *Table 2.6* lists the measured hardness values before and after LSP is performed. The strain hardening that occurs during LSP increases the measured hardness about 14%.

Condition	Vickers Hardness (average)
<u>Unpeened</u> (Annealed)	84.2
<u>Peened</u> (Annealed)	95.7
% Difference	14% increase

Table 2.6 – Vickers hardness of AZ91D before and after LSP

Chapter 3: Finite Element Analysis Modeling and Simulation

A Finite Element Analysis (FEA) model was developed to simulate the effects of Laser Shock Peening on the material characteristics of magnesium alloy AZ91. The objective in the development of the FEA model is to be able to accurately simulate the LSP process to predict residual stresses and deformations.

3.1 Pressure Pulse Model

A pressure model was developed in MATLAB to simulate the pressure load that the material experiences during LSP. The pressure pulse is determined using the power density calculated from the recorded LSP parameters/results (laser pulse-width, laser energy, and spot diameter).

Fabbro et. al. has developed an analytical model to describe the conversion of laser intensity to a pressure pulse with a SRT peak followed by a Gaussian profile distribution [22, 23, 26]. This model describes the process in three parts: (1) a shock wave is generated during the laser pulse duration that propagates into the confining material, (2) after the laser is shut off, the plasma maintains a pressure that decreases due to adiabatic cooling, which contributes to the impulse momentum, and (3) the expansion of heated gas inside the interface adds more momentum to the target [22, 23, 26].

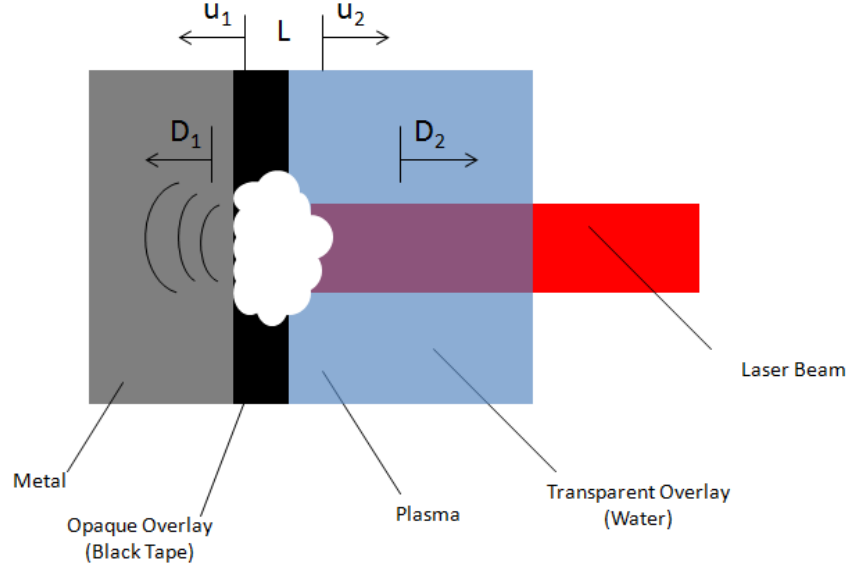


Figure 3.1 – LSP physical process

Figure 3.1 is an illustration of the physical process that takes place, where $L(t)$ represents the thickness of the plasma at time t , and u_1 and u_2 represent fluid velocities created by the two shockwaves [22, 23, 26]. These can be represented with the following expressions:

$$L(t) = \int_0^t [u_1(t) + u_2(t)] dt \quad (3.1.1) [22]$$

$$P = \rho_i D_i u_i = Z_i u_i \quad (3.1.2) [22]$$

where $P(t)$ represents the pressure at time t , ρ_i is mass density, D_i is shock velocity, and Z_i is shock impedance of the material in the direction of the shock wave. If the two media are considered to be solids, the shock wave impedances are:

$$Z_i = \rho_i D_i \quad (3.1.3) [22]$$

From these, we are able to obtain the following:

$$\frac{dL(t)}{dt} = \frac{2}{Z} P(t) \quad (3.1.4) [22]$$

Where,

$$\frac{2}{Z} = \frac{1}{Z_1} + \frac{1}{Z_2} \quad (3.1.5) [22]$$

If the two media are perfect gases, it is known that:

$$D_i = \left(\frac{(\gamma+1) P}{2 \rho_i} \right)^{1/2} \quad (3.1.6) [22]$$

And the pressure can be represented by:

$$P(t) = K \left(\frac{dL(t)}{dt} \right)^2 \quad (3.1.7) [22]$$

With

$$K = (\gamma + 1) \frac{\rho_o}{8} \quad \text{and} \quad \frac{2}{\rho_o^{1/2}} = \frac{1}{\rho_1^{1/2}} + \frac{1}{\rho_2^{1/2}} \quad (3.1.8) [22]$$

During the heating phase, the absorbed laser energy is used to increase the internal energy of the plasma. During the time interval dt , the plasma thickness increases by dL . The external energy of the laser applied to the system, $I(t)dt$ in energy per surface area, increases the internal energy $E_i(t)$ per unit volume and the work of the pressure loads $P(t)dL$. This is described by:

$$I(t) = P(t) \frac{dL}{dt} + \frac{d[E_i(t)L]}{dt} \quad (3.1.9) [22]$$

During this phase, only a constant fraction of the internal energy is thermal energy $E_T(t)$. This fraction, α , is used to represent the ionization of the gas. For an ideal gas, the thermal energy is related to the pressure by:

$$P(t) = \frac{2}{3} E_T(t) = \frac{2}{3} \alpha E_i(t) \quad (3.1.10) [22]$$

So Eq. 3.1.10 becomes:

$$I(t) = P(t) \frac{dL(t)}{dt} + \frac{3}{2\alpha} \frac{d}{dt} [P(t)L(t)] \quad (3.1.11) [22]$$

Combining these equations, we arrive at the following non-linear differential equation [22]:

$$\frac{d^2 L(t)}{dt^2} = I_p - \frac{\left(\frac{Z}{2} + \frac{3Z}{4\alpha} \right) \left(\frac{dL(t)}{dt} \right)^2}{\frac{3Z}{4\alpha} L(t)} \quad (3.1.12) [22]$$

For all FEA modeling of LSP, equation (3.1.12) is solved in MATLAB using the built-in Runge-Kutta differential equation solver to obtain the pressure pulse load history applied to the material. The inputs to solve the equation are laser intensity (power density), pulse width, material impedances, initial plasma thickness, and the thermal energy conversion factor α .

3.2 Material Model

The Johnson-Cook (JC) material model is used to represent the strength behavior of materials subjected to large strains, high strain rates and high temperatures on a macroscopic level. This behavior can occur in problems of intense impulsive loading due to high velocity impact and explosive detonations, similar to LSP. The model represents three material responses: strain hardening, strain-rate effects, and thermal softening [27]. At the high strain rates that occur during LSP, a material's yield strength will increase with time.

The constitutive equation for the Johnson-Cook model defines the yield strength as:

$$\sigma_Y = [A + B(\varepsilon_p)^n](1 + C \cdot \ln \dot{\varepsilon})[1 - (T_H)^m] \quad (3.2.1) [27]$$

ε_p = effective plastic strain

$\dot{\varepsilon} = \frac{\varepsilon_p}{\dot{\varepsilon}_o}$, where $\dot{\varepsilon}_o$ is strain rate used to determine constants A , B , and n

T_H = the homologous temperature, where

$$T_H = \frac{T - T_R}{T_M - T_R} \quad (3.2.2) [27]$$

T_M = melting temperature

T_R = reference temperature when determining A , B & n

$$\Delta T = \frac{1}{\rho C_p} \int \sigma d\varepsilon_p \quad (3.2.3) [27]$$

ρ = mass density

C_p = specific heat

In the constitutive model, A , B , n , C , and m are the model parameters, and ρ , C_p , and T_M are the material characteristics. A is usually the initial yield stress of the material, B is related to the increase in strength due to work hardening of the material, n is the work hardening coefficient, and C is related to the strain rate sensitivity of the material [28]. The m parameter is the homologous temperature coefficient, which has little to no effect during LSP since we are using opaque and transparent overlays, making it purely a mechanical process.

The Johnson-Cook model also uses the material elastic parameters, which are put into an Equation-of-state (EOS). The EOS is used to define pressure vs. volume strain response, and is usually defined by the bulk modulus of the material.

A cumulative-damage fracture model is also included in the Johnson-Cook material model. This is defined as:

$$\varepsilon^F = \left(D_1 + D_2 \exp \left[D_3 \frac{P}{\sigma_{eff}} \right] \right) (1 + D_4 \ln \dot{\varepsilon}) (1 + D_5 T_H) \quad (3.2.4) [27, 28]$$

$$D = \sum \frac{\Delta \varepsilon_{eff}^p}{\varepsilon^F} \text{ failure occurs when } D=1$$

σ_{eff} = effective stress

P = mean stress (pressure)

The cumulative-damage fracture model can be neglected because the material is not experiencing permanent damage or fractures. In the case of LSP, the damage model is only required when analyzing spallation effects from LSP. The effects of thermal softening can also be neglected since the material will not experience high temperatures during peening.

3.3 FEA Model – Pre-processing

The Johnson-Cook model described in Chapter 3.2 has been incorporated into an explicit 3-D model using the commercial FEA program LS-DYNA to analyze the effects of LSP on the residual stress validated by experimental results. The simple case of single-shot LSP on a large target of AZ91D will be analyzed. The model will simulate double-sided LSP since we have only been able to obtain compressive residual stresses using that method. The test specimen (from experimental results) used for model calibration was 20mm x 20mm with a 2.85mm thickness. The LSP conditions were recorded and are listed in *Table 3.1* and the stress depth profiles can be seen in *Figure 3.2*. Since double-sided LSP was performed, average values from each channel of the laser are shown and used in the simulation.

Side	Spot Dia.	Energy	Pulse Width	Power Density	Measured Surface Stress
Coupon 1	2.3mm	4.76 J	21.14 ns	5.42GW/cm ²	-153.91 MPa
Coupon2	2.4mm	2.23 J	28.8 ns	1.71 GW/cm ²	-113.36 MPa

Table 3.1 – Model calibration specimen LSP parameters

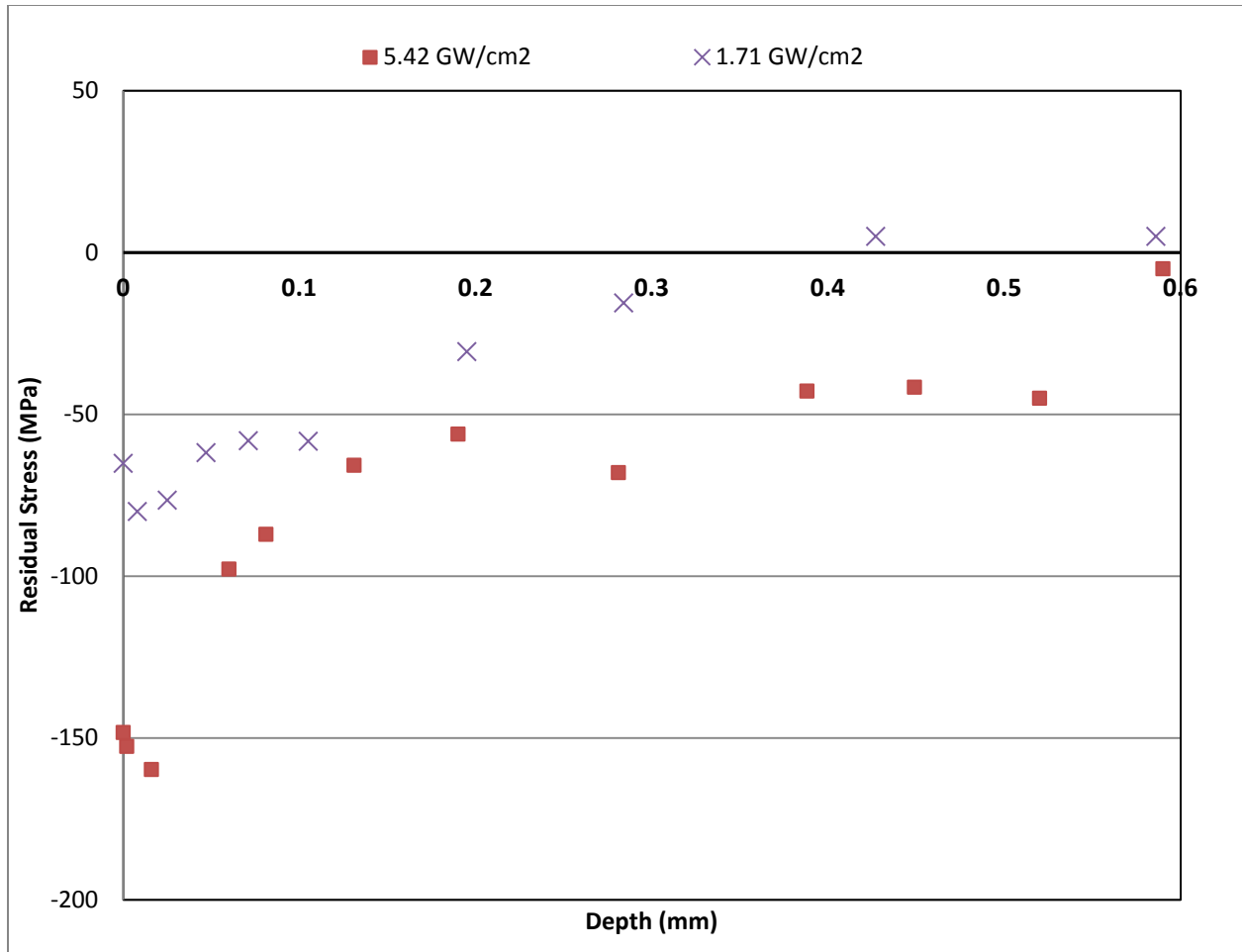


Figure 3.2 – Residual stress depth profile target for simulation

3.3.1 Meshing and Geometry

A simple model was created and meshed in Hypermesh. The geometry of the specimen used was 10mm x 10mm x 2.85mm to reduce computation time. The model was meshed using 8-node, constant stress brick elements. A relatively fine mesh was used with 10,000 elements per layer and 60 elements through the thickness. A bell curve node count was used to create a higher element count close to the LSP surfaces so the near-surface residual stress effects could be observed. The model is shown in *Figure 3.3*.

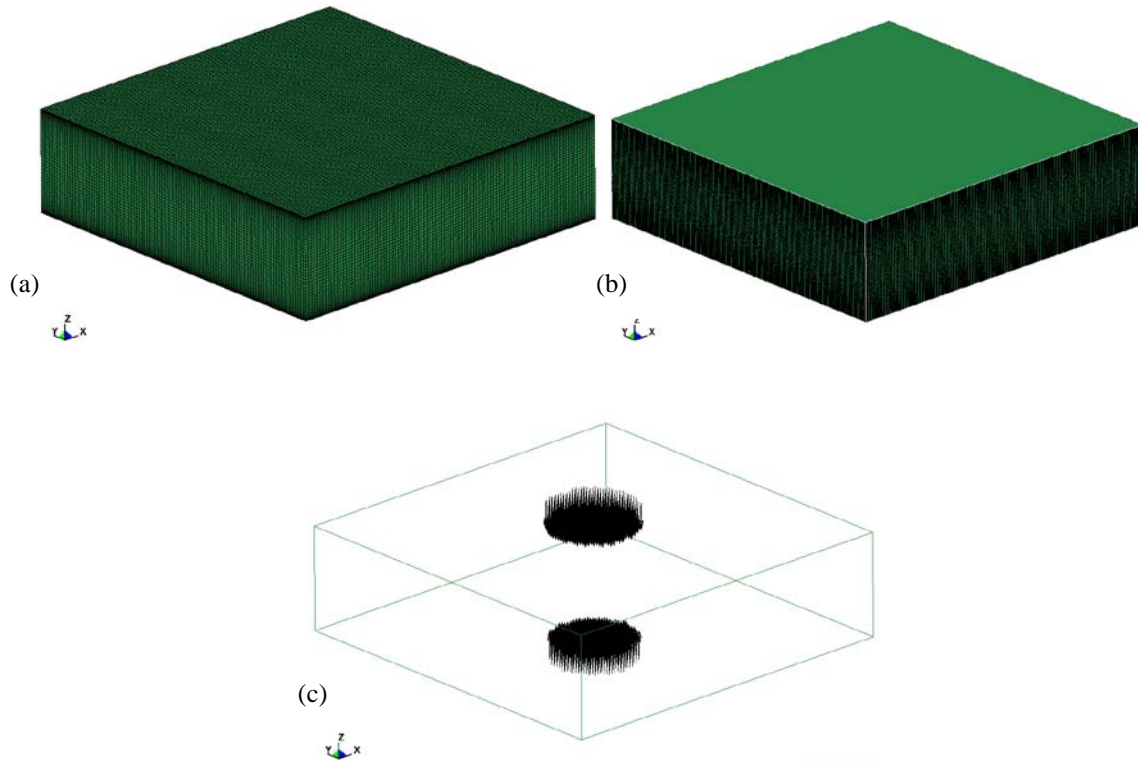


Figure 3.3 – Model Setup (a) meshed 3-D Model, (b) non-reflecting boundary conditions, (c) loads

3.3.2 Boundary Conditions

Boundary conditions are an important factor in modeling LSP. In the test environment, the LSP specimen is usually clamped or held fixed by a robot. When simulating multiple shots, smaller specimens, and single-sided LSP an accurate representation of the boundary conditions is important. Since a larger test specimen was used and the constraints are far away from the LSP spot in this case, it is reasonable to consider a semi-infinite domain around the edges of the of the coupon. This is applied in LS-DYNA as a non-reflecting boundary condition, which is represented by the shaded region in *Figure 3.3 (b)*.

3.3.3 Applied Loads

The pressure pulse generated during LSP is likely the most important factor in the model. Since we are modeling double-sided LSP, the loads applied will be even more important because

a slight variation can have a dramatic effect on the results. Using the LSP parameters listed in *Table 3.1*, a pressure pulse was generated in MATLAB using the Runge-Kutta differential equation solver. The inputs to solve the equation are laser intensity (power density), pulse width, material impedances, rise time, initial plasma thickness, and the thermal energy conversion factor α . The intensities and pulse widths recorded from each channel are listed in *Table 3.1*. Material impedances are known for the transparent overlay (water) and the opaque overlay (black tape). The rise time for the SRT peak for this laser is assumed to be 5 ns. The thermal energy correction factor, α , was set to 1.0. Note that this factor is now calibrated to match the residual stress and therefore it does not have clear physical meaning. Once the material model is calibrated, a variation study will be done to examine the effects of the thermal energy correction factor. *Figure 3.4* shows the laser pressure pulses generated from the MATLAB code. The loads generated were input into LS-DYNA as a time history curve. The control time step was adjusted to be lower than the smallest time step in the pressure pulse history-curve so that each load step would be captured in the analysis.

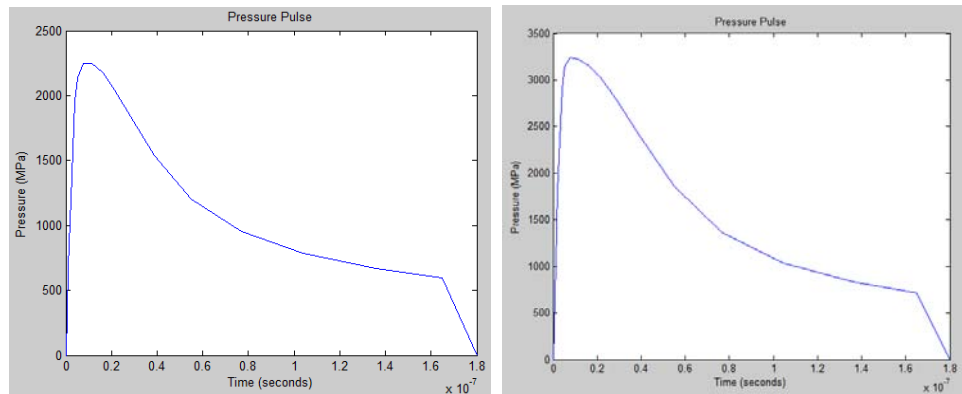


Figure 3.4 – Pressure pulse time history (a) 5.42 GW/cm², 21.14 ns, (b) 1.71 GW/cm², 28.8 ns

The next step in the pressure model is to create a load area. This is done using a MATLAB code that uses the LSP spot radius and center location on a given surface and creates

the loads around the center point. In order for the code to work properly, an element set segment on the surface of interest is defined in LS-DYNA and output to a text file along with the nodal coordinates of that set. This must be done separately for each surface since they have different diameters and loads. During this step, there is an option of a spatial distribution of the loads or uniform distribution. Since the Veeco analysis shown in *Figure 2.10* shows very little spatial distribution, a uniform load distribution shall be used in this analysis.

3.3.4 Damping

The final step in the model setup is to create a damping model. After the loading process, a restart analysis file is read to provide material damping near the critical damping value of the material. This is done to dampen any transient elastic effects created during the loading process in an efficient manner, which will result in a steady state solution. The damping coefficient for this material is set to 10^6 and the restart analysis is run for 10^{-4} seconds to allow enough time for the material to fully dampen.

3.3.5 Runner Script

The model is run on a LINUX computing system. A runner script has been developed that will run the full simulation with the LS-DYNA *.k input files. First it runs the LSP process, then a restart analysis with the damping input file. This script can also be used to run multiple shot simulations and patches. The simulation time for the model to complete is about one hour.

3.4 Post-processing

Once the simulation has been completed, the results files are transferred to a local machine and viewed in LS-PrePost. We are interested in the σ_x and σ_y residual stresses created from LSP. These stresses are defined in LS-DYNA as X-STRESS and Y-STRESS. To create the plot for RS, a MATLAB code was developed. This code requires the elements inside the LSP dimple to be selected. The element stress results are then written to a text file. The

MATLAB code requires the number of elements per layer and the number of elements through the depth as inputs. It uses these to average the stress for each layer of elements through the depth and creates the stress-depth profiles. Since LXRD measurements used a 1mm diameter aperture to measure residual stresses experimentally, a 1mm x 1mm region of elements is selected for the stress-depth profile.

Chapter 4: FEA Results

4.1 Material Model Parameter Study

In order to obtain an acceptable material model, the modeling results must closely match experimental results for deformations, in-plane surface stress, and stress-depth profiles. In this study, the Johnson-Cook material parameters were adjusted so that that these conditions were met.

The Johnson-Cook model described in Section 3.2 was implemented in LS-DYNA with a built-in material model. LS-DYNA has two built-in material models for Johnson-Cook. Since LSP is a purely mechanical process, we are only concerned with the strain rate and hardening effects. We will use material model 098-SIMPLIFIED_JOHNSON_COOK since it neglects the effects of thermal softening, leaving the Johnson-Cook model with the following representation.

$$\sigma_Y = [A + B(\varepsilon_p)^n](1 + C \cdot \ln \dot{\varepsilon}) \quad (4.1.1)$$

Table 4.1 lists the known material properties required for the model. The model parameter, A, can be considered as the initial yield stress of the material, which is set to 160 MPa. Ulacia et. al. developed a Johnson-Cook material model for Mg alloy AZ31B through experimental methods [28]. However, the strain rates they used in testing were on the order of 10^3 s^{-1} , which is too low to be compared to LSP, which can reach strain rates on the order of 10^6 s^{-1} . This means that their model for Mg alloys may not be a great reference point.

AZ91 Material Properties	
Modulus of Elasticity	45 GPa
Shear Modulus	17 GPa
Poisson's Ration	0.35
Yield Stress	160 MPa
Density at 20°C	1.81 g/cm ³

Table 4.1 – AZ91 material properties

Since the University of Cincinnati has developed a material model to simulate LSP on titanium (*Table 4.2*), this can serve as an initial reference point in the material model development with the initial yield stress, A, set to 160.

Initial Reference Johnson-Cook	
A	160
B	1092
n	0.4
c	0.04

Table 4.2 – Initial reference

Using the initial reference as a baseline, the material parameters were varied individually until an accurate fit of the stress-depth profile was reached. This fit is shown in *Figure 4.1*. The validated Johnson-Cook material parameters used to reach this fit are listed in *Table 4.3*. The fringe plots of the residual stress are shown in *Figure 4.2* and *4.3*. The residual stress effects are identical in both the x and y direction (σ_x and σ_y).

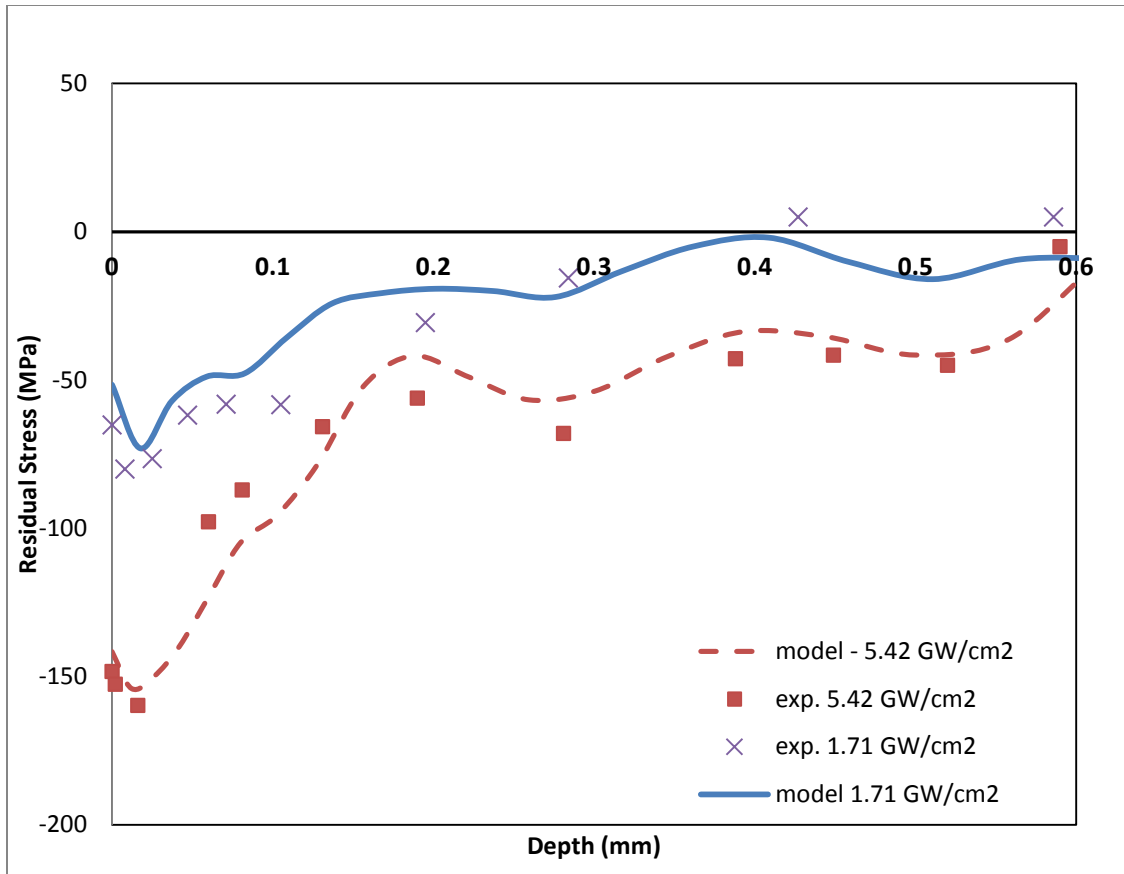


Figure 4.1 – Stress-depth profile FEA model validation

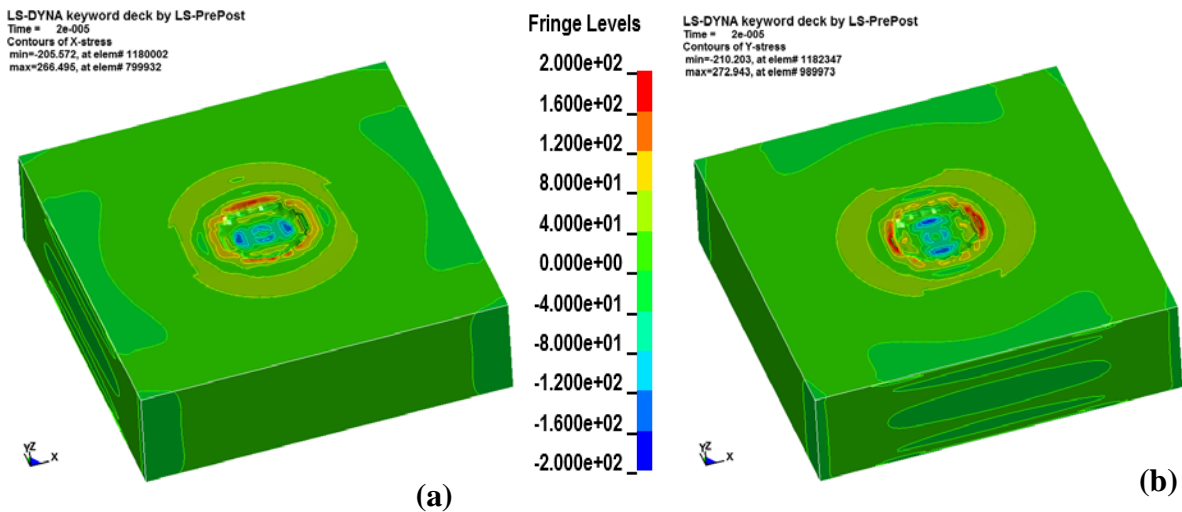


Figure 4.2 – Residual stress of single shot, double sided LSP of (a) σ_x and (b) σ_y in MPa

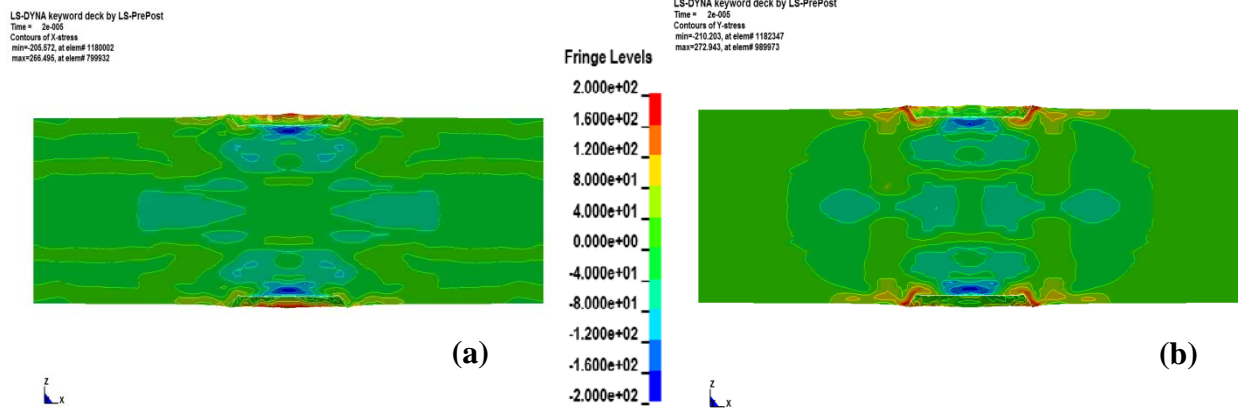


Figure 4.3 – Through-depth residual stress (a) σ_x and (b) σ_y in MPa

Validated Johnson-Cook Parameters	
A	80 MPa
B	346 MPa
n	0.35
c	0.02

Table 4.3 – Validated Johnson-Cook parameters for Mg Alloy AZ91D

Figure 4.3 shows the profile of the dimple displacement from the LS-DYNA model overlaid with the experimental data recorded from Veeco analysis. The dimple profile shape closely matches the dimple profiles recorded from the Veeco measurements shown in Figure 2.10. The dimple depth from the LS-DYNA is about $120 \mu\text{m}$, while the dimple depth recorded during experimentation is about $100 \mu\text{m}$. Since the dimple depth is off by about $20 \mu\text{m}$, some future adjustments may be required to the hardness parameters of the model to reach more accurate values for displacements. There also appears to be a spike at the edges of the dimple in the LS-DYNA model. Since this spike does not appear as significant in the Veeco data, a finer mesh may be required to obtain a more accurate dimple profile.

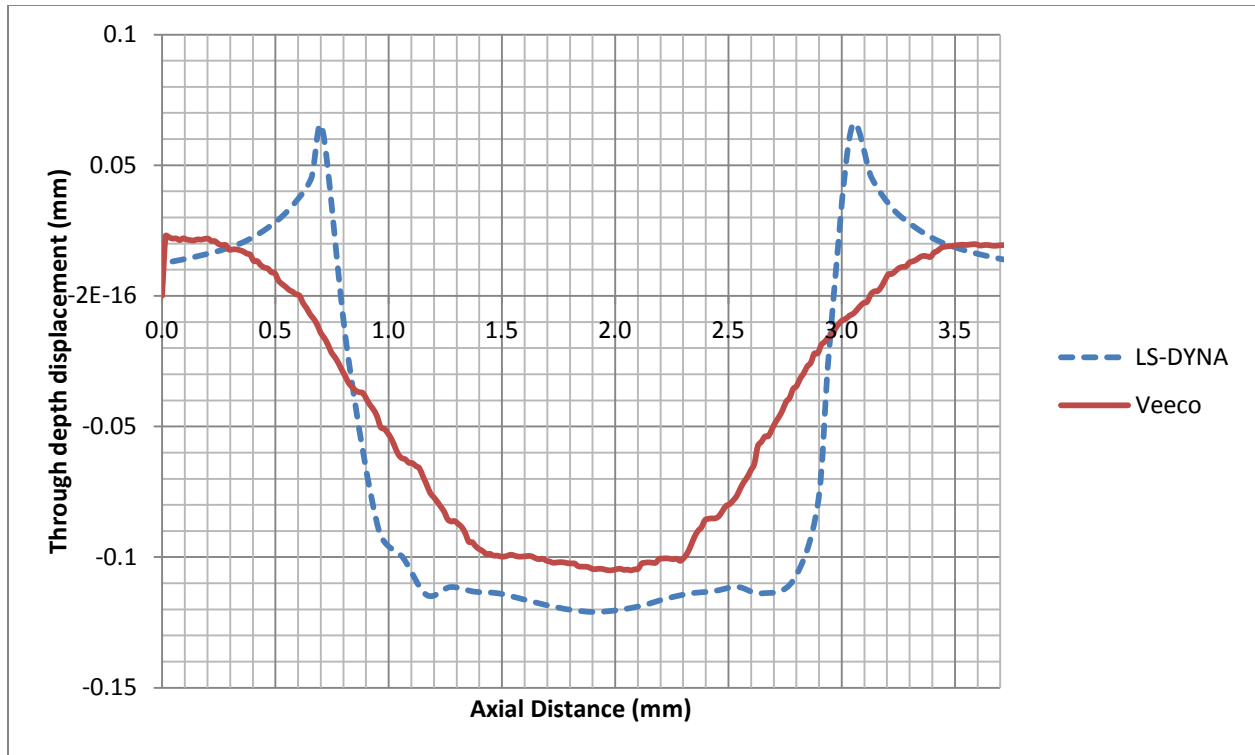


Figure 4.3 – Dimple depth comparison

Since the data from the LS-DYNA model accurately matches the experimental data, it can be concluded that the Johnson-Cook parameters listed in *Table 4.3* can be used as an accurate representation of the material behavior of Mg alloy AZ91D during the LSP process.

4.2 Thermal Energy Conversion Factor (α) Variation Study

The thermal energy conversion factor (α) from equation (3.1.12) is important in determining the pressure pulse that the material experiences during LSP. Varying this parameter slightly can result in much different pressure pulse profiles. This is a difficult aspect to verify experimentally, so modeling can be helpful in determining the value of α . Since the laser used for all experimentation in this thesis is relatively old and inefficient, it is even more difficult to determine the actual value of α .

A variation study was performed on the same model used for the Johnson-Cook parameter-study to understand the effects of the thermal energy correction factor. Since α was set to 1.0 for the Johnson-Cook parameter-study that can be used as a baseline. The variation values for α in this study were 0.1, 0.5, 0.8, and 1. The pressure pulses from each variation are shown in *Figure 4.3*.

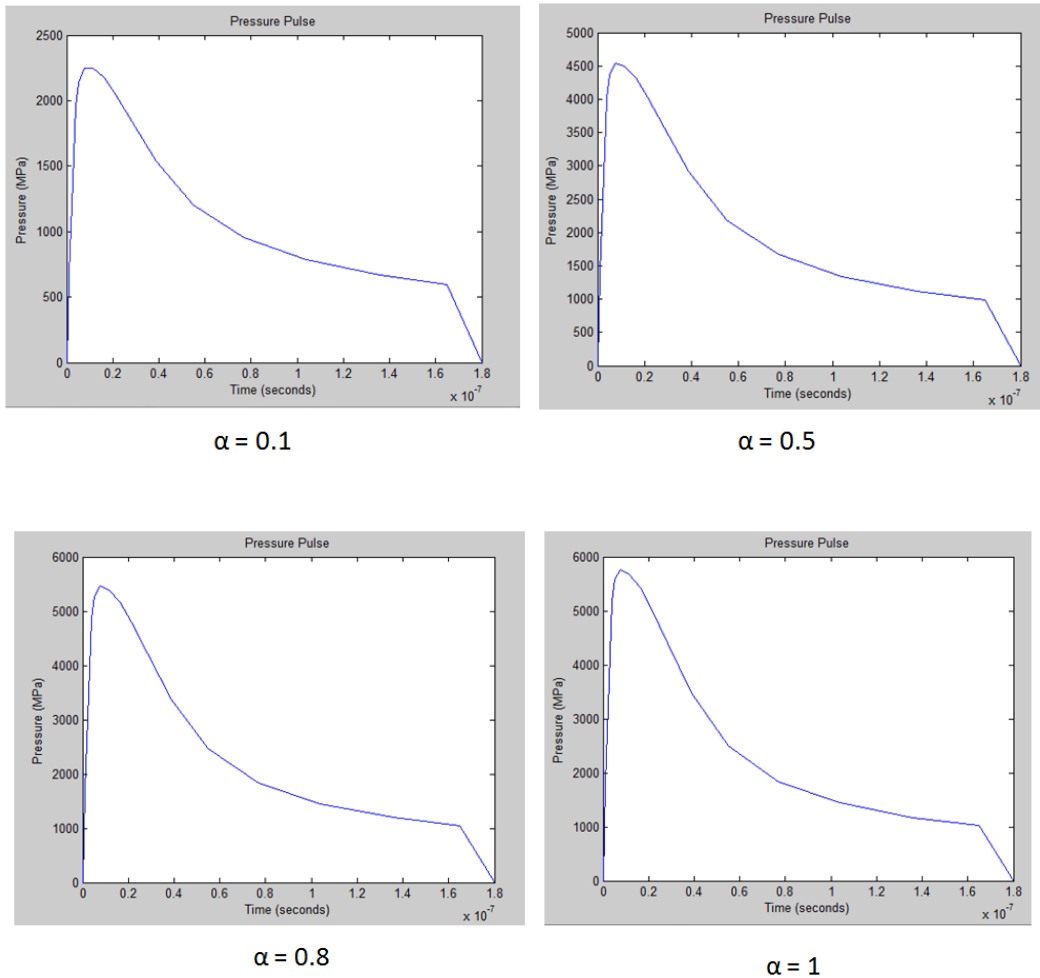


Figure 4.3 – Alpha pressure pulse variation

The results of the thermal energy variation study are shown in *Figure 4.4*. The figure shows the residual stress through a 1mm depth of the specimen. It can be seen that for lower values of alpha, the residual stress at the surface is smaller, but increases near the center of the

coupon. For higher values of alpha, the compressive residual stress is larger near the surface and decreases near the center of the sample.

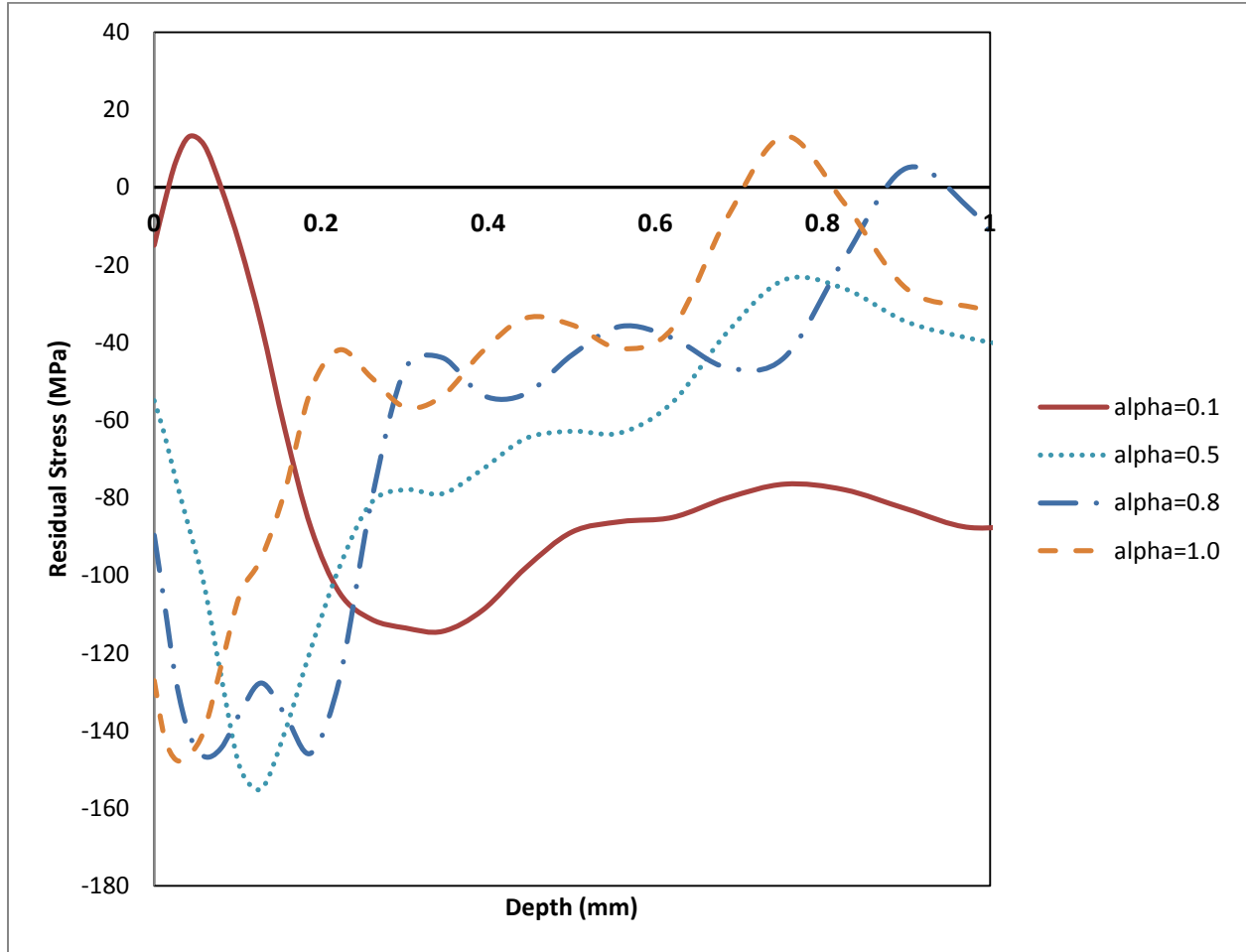


Figure 4.4 – Alpha variation stress-depth results

From this data, it can be concluded a value of 1.0 is the best value to use for the thermal energy correction factor.

4.3 Finite Element Model Conclusions

The implementation of FEA methods to simulate the effects of LSP on the residual stress of AZ91D was successful. The LS-DYNA model was effective in simulating the LSP process. A material model was developed that accurately represents the material behavior of AZ91D observed in experimentation, including the plastic deformation and residual stress profiles.

Varying the thermal energy conversion factor (α) can significantly change the material response from LSP. This model will require future efforts with more detailed experimental data. If the material model proves to be inconsistent, it may require the development of a new material model or a micro-scale material model.

Chapter 5: Experimental Methods

5.1 DC Polarization Test

Electrochemical corrosion tests can be used to evaluate the corrosion characteristics of a material for *in vitro* applications. A DC polarization test is a common electrochemical corrosion test that is capable of measuring the corrosion potential and corrosion current of metals.

5.1.1 Theory

The DC polarization test requires a known surface area of the test specimen to be exposed to the corrosive fluid. A reference electrode, which is attached in parallel with the test specimen, acts as the anode and applies an external current to the system and polarizes the cathodic elements [29, 30]. A counter electrode acts as the cathode as the current flows out of the system [29, 30]. The open circuit potential and the corrosion current can be determined from this test. *Figure 5.1* shows a DC polarization model.

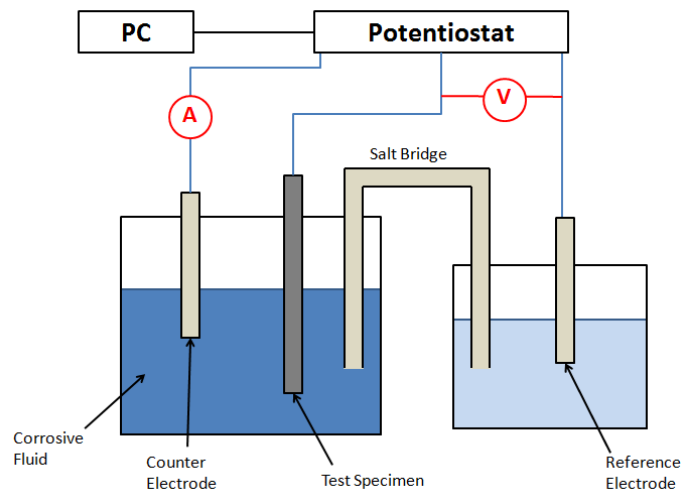


Figure 5.1 – DC polarization model

The DC Polarization test is known as a voltammetric technique and generates a current vs. voltage curve under conditions of concentration polarization. The test involves a potential scan of the test specimen immersed in the corrosive fluid and creates the current-voltage curve,

which is known as a Tafel plot. The Tafel plot can be used to determine corrosion rates, passivation currents, resistance to pitting and the effectiveness of corrosion inhibitors [29]. The corrosion rate can be determined using Linear Polarization Resistance method over a potential range near the corrosion potential of the material. This requires sweeping the potential of the working electrode at a fixed scan rate and measuring the current.

Figure 5.2 shows a typical Tafel plot. The open circuit potential (E_{corr}) and current density (I_{corr}) can be determined by taking the slopes of the anodic and cathodic regions and finding where they intersect [29, 30].

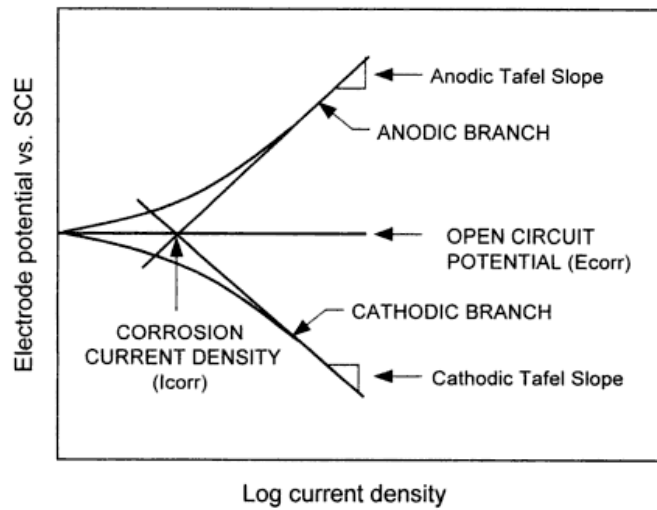


Figure 5.2 – Tafel plot (from [29])

Once the corrosion current density is known, it can be combined with Faraday’s law:

$$W = \frac{M \cdot Q}{nF} \quad (5.1.1) [30]$$

$$Q = I_{corr} \times \text{time} \quad (5.1.2) [30]$$

where W is the weight or mass of material removed [g], M is the molecular weight [g] of the test specimen, Q is the total charge passed [coulombs], n is the number of electrons transferred in the

reaction, and F is Faraday's constant [96,485.345 coulombs]. Once the weight of the material is known, the rate of corrosion can be calculated as follows:

$$\text{Corrosion Rate} = \frac{W * SA}{\rho} \quad (5.1.3) [30]$$

where W is the weight of the material removed [g], SA is the exposed surface area [cm²], and ρ is the mass density of the material [g/cm³]. To simplify the system, the following equation can be used to determine the corrosion rate in milli-inches per year.

$$C.R. (mpy) = \frac{0.13 I_{corr}(E.W.)}{\rho} \quad (5.1.4) [30]$$

where I_{corr} is the current density [$\mu\text{A}/\text{cm}^2$] and E.W. is the equivalent weight of the specimen [g]. The lower the corrosion current density, the lower the corrosion rate will be.

5.1.2 Methodology

All test specimens must be smooth and free of any surface impurities. Surface roughness has been shown to have a negative effect on the corrosion rate of many materials. In order to avoid this, all samples must be polished to a mirror finish prior to LSP and testing. Water can cause microscopic pitting on the surface of magnesium or magnesium alloys, so ethanol must be used during polishing procedures.

The purpose of this test is to determine the effects of LSP, specifically residual stress, on the corrosion characteristics of AZ91D. Single LSP shots are the best way to determine the local effects of residual stress, since the RS can be measured in that region and will remain relatively consistent around the dimple. Double-sided LSP will be performed on the test specimens, since it has been determined that it is the best way to achieve compressive residual stress on AZ91D. After LSP, the residual stress of each spot must be measured and recorded.

To determine the actual effects of residual stress, a range of surface residual stresses must be tested. Same tests are performed on unpeened samples. After LSP is performed on the coupons and the RS is measured, the test specimens are selected based on the measured surface RS to capture a good range.

In order to properly execute a DC polarization corrosion test, the surface area exposed to the corrosive fluid must be known. During testing, the sample must be blanked off with the exception of the exposed spot. This is done using non-conducting tape and is explained in the test procedure.

The corrosive fluid chosen for the experiment is saline (0.9% NaCl). Saline solutions are commonly used for *in vitro* corrosion test applications because they are considered to accurately simulate the *in vivo* corrosive environment.

5.1.3 Procedure

5.1.3.1 Coupon Preparation

AZ91D plates were heat treated at 400°C for 24 hours and air cooled at room temperature. AZ91D plates were cut into 15mm x 100mm x 3mm coupon using Electrical Discharge Machining (EDM).

In order to avoid effects of surface roughness and impurities on corrosion, all test specimens were polished to a mirror finish. Each coupon was finely polished using silicon carbide 1200 fine grit paper while overlapping with ethanol. Each coupon was then polished to a mirror finish with a TexMet® Microcloth using Buehler™ 1µm diamond polishing solution while overlapping with ethanol. Total polishing procedure lasts about 30 minutes per coupon.

Residual stresses were measured on each coupon prior to LSP using the Proto™ LXR D Stress Measurement System. Residual stresses prior to LSP were observed to be approximately 0 MPa.

5.1.3.2 LSP Procedure

Double-sided LSP was performed on each test specimen. During LSP, each test specimen was secured at one end as shown in *Figure 5.3*. Black tape was placed on each side of the coupon to act as the opaque overlay. Water was run on each side of the specimen, over top of the tape, at a constant stream with a thickness of approximately 2 mm. Five (5) single LSP shots were performed on each coupon, with the laser firing simultaneously on each side of the coupon. Spacing between shots was 15mm center-to-center. Images of the LSP set up can be seen in *Figure 5.3*.

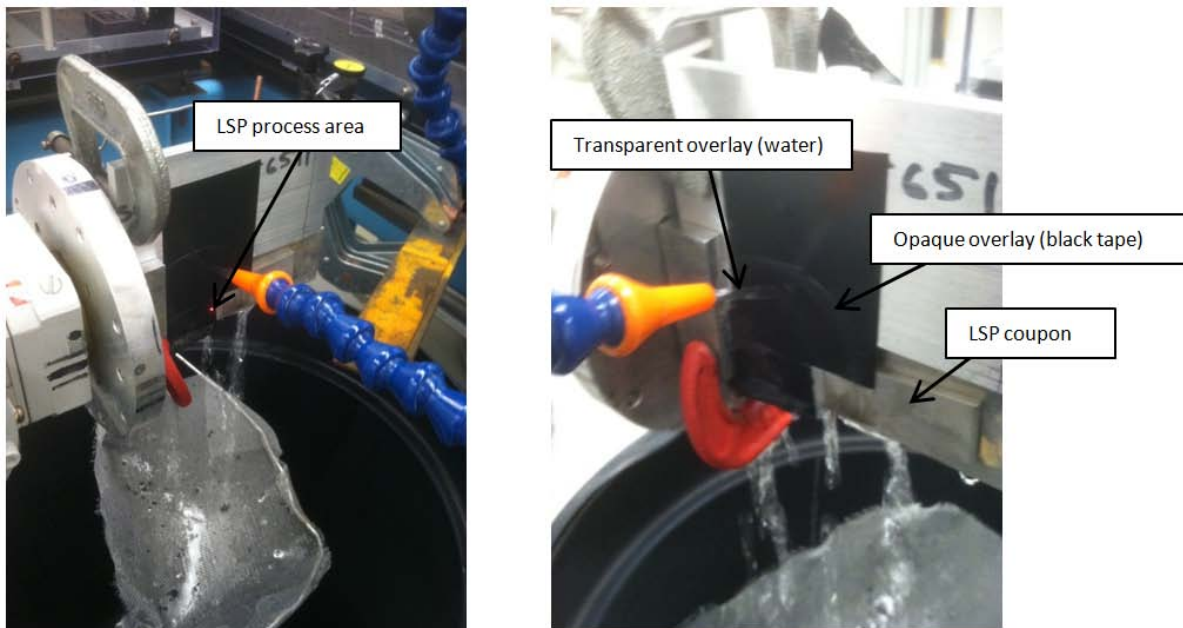


Figure 5.3 – LSP application arrangement

After LSP, each dimple was marked with a designation using an engraver and the corresponding LSP parameters were recorded from each laser channel (side) for each shot. The

recorded parameters are pulse width (ns) and laser energy (J). After LSP, a quick scan using the Veeco™ Profilometer was performed to determine the approximate dimple diameter created from each shot so that the power density could be calculated.

Next, the surface in-plane residual stresses were measured for each dimple using the Proto™ LXRDR Stress Measurement System and the LXRDR parameters listed in *Table 2.3*. Each stress measurement was recorded along with the corresponding spot designation.

5.1.3.3 DC Polarization Test Procedure

A DC Polarization Corrosion Test was performed on the LSP spots. The DC Corrosion test was performed using a Gamry potentiostat with DC105™ DC Corrosion Techniques Software used to evaluate the corrosion on the LSP spots. All corrosion tests were performed following the test procedure.

In order to properly execute a DC polarization corrosion test, the surface area exposed to the corrosive fluid must be known. In order to do this, the rest of the test specimen was blanked off using black (non-conducting) tape, with the exception of a 3.8mm diameter hole around the area of interest that was cut from the tape using a hole-punch as shown in *Figure 5.4*.

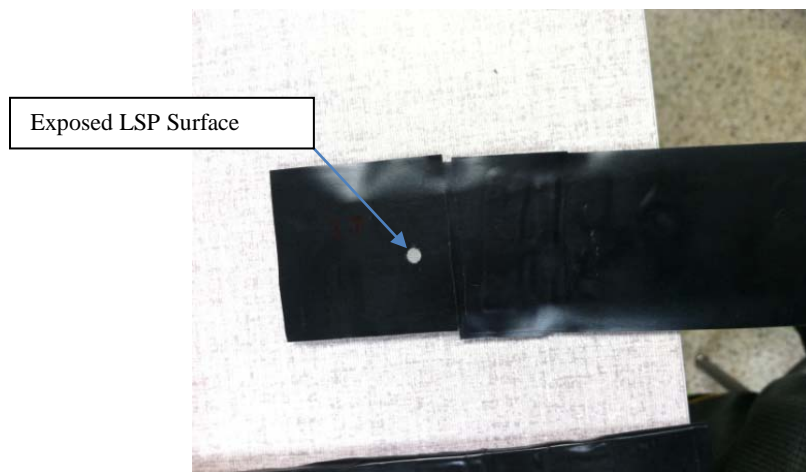


Figure 5.4 – DC corrosion test sample

The test setup is shown in *Figure 5.5*. The test cell was filled with a saline (0.9% NaCl) solution. The electrodes were attached to the appropriate resistors. The test specimen was aligned so that the exposed area of the coupon was within a 10mm diameter opening in the test cell. The coupon was then tightly secured against the wall of the test cell to prevent the fluid from leaking.

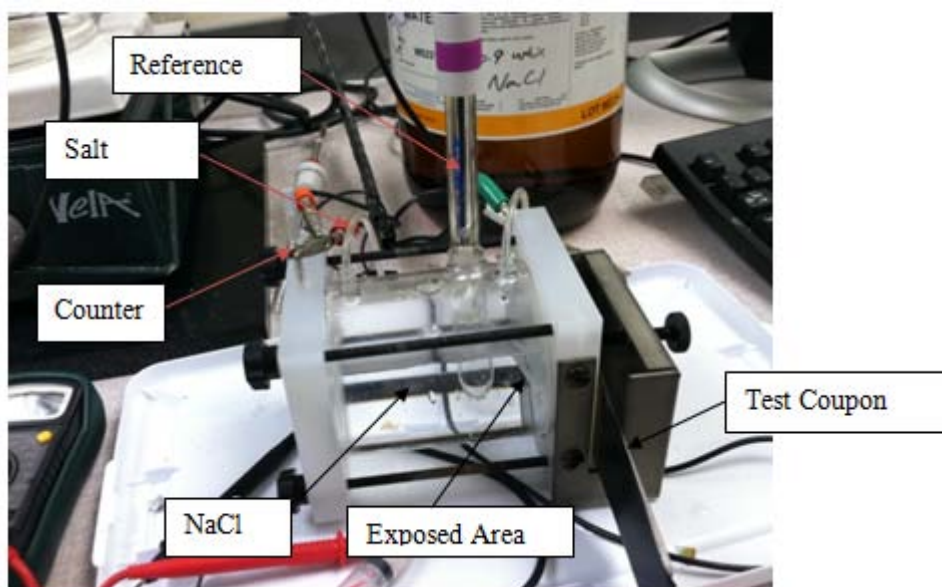


Figure 5.5 – DC polarization corrosion test setup

A Tafel scan was executed on each spot, which was used to obtain the kinetic parameters and the corrosion characteristics of the material. All data was given the assigned the appropriate designation for each LSP spot so that the data could later be analyzed.

5.2 Immersion Corrosion Test

Another common way to evaluate the corrosion resistance of a material is through an immersion test. Immersion tests can be used to evaluate corrosion resistance via weight loss measurements over time while a sample is completely immersed in a corrosive fluid.

5.2.1 Theory

The purpose of the immersion test is to physically evaluate the weight loss of a specimen immersed in a corrosive fluid over a known period of time. In order to properly measure the corrosion rate, the mass of the sample must be recorded before and after the test. The weight loss is usually measured in intervals over the immersion period to record the corrosion rate at different times. The corrosion rate can be calculated with the following equation:

$$C.R. = \frac{K(W_i - W_f)}{\rho A \Delta t} \quad (5.2.1)$$

where W_i is the initial weight of the sample, W_f is the final weight, ρ is the mass density, A is the exposed surface area, Δt is the change in time, and K is a constant for unit conversion. In this case the weight is measured in grams and K is 8.75×10^4 to get the corrosion rate in millimeters per year.

5.2.2 Methodology

All test specimens must be smooth and free of any surface impurities. Surface roughness has been shown to have a negative effect on the corrosion rate of many materials. In order to avoid this, all samples must be polished to a mirror finish prior to LSP and testing. Water can cause microscopic pitting on the surface of magnesium or magnesium alloys, so ethanol must be used during polishing procedures.

The purpose of this test is to determine the effects of LSP, specifically residual stress, on the corrosion characteristics of AZ91D. Single LSP shots are the best way to determine the local effects of residual stress, since the RS can be measured in that region and will remain relatively consistent around the dimple. Double-sided LSP will be performed on the test specimens, since

it has been determined that it best way to achieve compressive residual stress on AZ91D. After LSP, the residual stress of each spot must be measured and recorded.

Similar to the DC polarization test, a known surface area must be exposed to the corrosive fluid during an immersion test. However, since the sample must be completely immersed in the fluid and a localized residual stress is known, the test specimen preparation process is slightly more complicated. All test specimens for the immersion corrosion tests are set in a non-conducting epoxy mount for the tests. The mounts must be non-conducting so that a galvanic couple is not created during the corrosion test. Galvanic couples can inhibit the corrosion rate of the test sample.

In order to do this, individual samples for the dimple must be cut from the coupon after LSP is performed. Although it would be ideal to cut the samples using EDM due to its accuracy and capability of cutting without imparting any significant amount of additional residual stresses to the sample, it requires that the coupon be immersed in water during the cutting process. As previously mentioned water can cause microscopic pitting and initiate some corrosion on magnesium and magnesium alloys. In order to avoid this, it was decided that the samples be cut from the coupon using a band saw. This caused some initial concern that the band saw might impart additional RS on the samples, but after some experimentation with this method prior to testing, it proved that no significant amounts of RS were created during the cutting process. The rest of the surface is blanked off using non-conducting tape, so that only the LSP surface is exposed to the fluid.

The corrosive fluid chosen for the experiment is a saline (0.9% NaCl). Saline solutions are commonly used for *in vitro* corrosion test applications because they are considered to accurately simulate the *in vivo* corrosive environment.

5.2.3 Procedure

5.2.3.1 Coupon Preparation

Coupon preparation details can be seen in section 5.1.3.1.

5.2.3.2 LSP Procedure

Double-sided LSP was performed on each test specimen. During LSP, each test specimen was secured at one end as shown in *Figure 5.3*. Black tape was placed on each side of the coupon to act as the opaque overlay. Water was run on each side of the specimen, over top of the tape, at a constant stream with a thickness of approximately 2mm. Five (5) single LSP shots were performed on each coupon, with the laser firing simultaneously on each side of the coupon. Spacing between shots was 15mm center-to-center. Images of the LSP set up can be seen in *Figure 5.3*.

After LSP, each dimple was marked with a designation using an engraver and the corresponding LSP parameters were recorded from each laser channel (side) for each shot. The recorded parameters are pulse width (ns) and laser energy (J). After LSP, a quick scan using the Veeco™ Profilometer was performed to determine the approximate dimple diameter created from each shot so that the power density could be determined.

Next, the surface in-plane residual stresses were measured for each dimple using the Proto™ LXR Stress Measurement System and the XRD parameters listed in *Table 2.1*. Each stress measurement was recorded along with the corresponding spot designation.

5.2.3.3 Mounting Procedure

After LSP was performed on the coupons and each LSP spot was designated, the individual dimples had to be set in epoxy mounts for the immersion tests. In order to do this, individual samples for the dimple had to be cut from the coupon. Each sample was cut using a band saw. The RS of each sample was measured after the cutting process to ensure that no additional stresses were created during the cutting process.

Once cut, each sample was placed in a non-conducting epoxy mount. Prior to mounting, tape was applied to the peened surface of each sample so that the epoxy solution would not harden over the test surface. Once mounted, the samples were ready for the immersion test.

5.2.3.4 Immersion Test Procedure

Similar to the DC polarization test, a known surface area must be exposed to the corrosive environment. In order to do this, the rest of the test specimen was blanked off using black (non-conducting) tape, with the exception of a 3.8mm diameter hole around the area of interest that was cut from the tape using a hole-punch as shown in *Figure 5.6*.

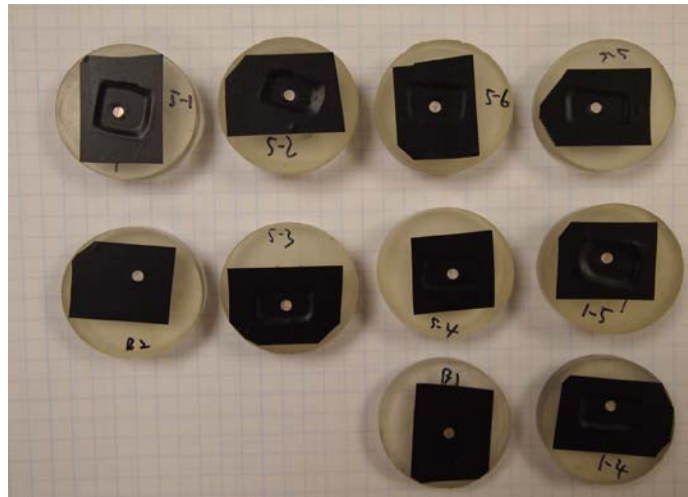


Figure 5.6 – Immersion test samples

The initial weight of the test specimens was measured prior to testing. The samples were then immersed in a saline (0.9% NaCl) solution. The immersion time was 200 hours. The weight loss of the samples was measured periodically during the test at 20 hours, 80 hours, 160 hours, and 200 hours. To better simulate the *in vivo* condition, the samples were dried, but not cleaned for each weight loss measurement.

Chapter 6: Experimental Results

The corrosion tests described in Chapter 5 were performed on a number of samples. As can be expected with any experiment, errors or inconsistencies can occur during testing which can have an effect on the results. As a consequence only a few data points were extracted from each corrosion test which yielded acceptable results.

6.1 DC Polarization Test Results

The DC polarization test was performed on nearly 20 LSP coupons, but many of the coupons read inaccurate data due to a low scan rate, a poor exposure area, or poor placement of the tape on the sample. *Figure 6.1* shows the Tafel plot for the data selected.

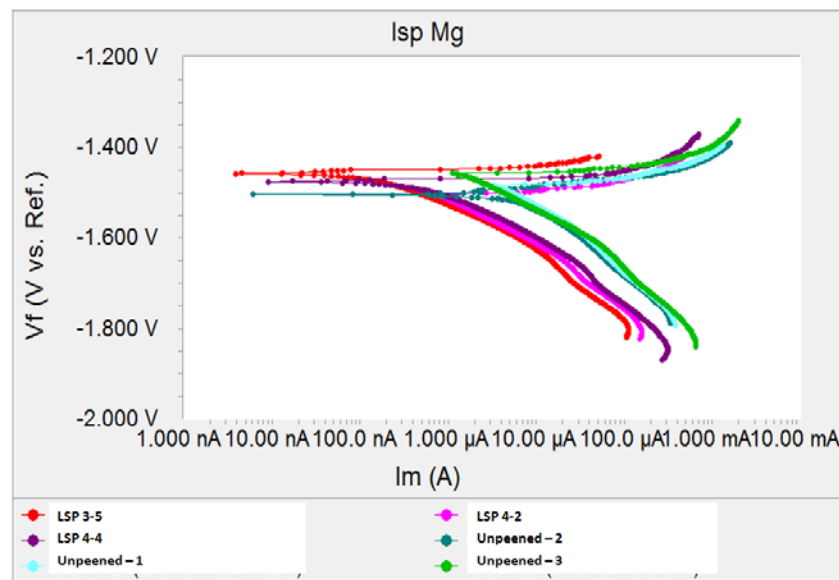


Figure 6.1 – DC polarization corrosion current vs. potential

As shown in *Figure 6.1*, there is an obvious shift to the left in the corrosion current for LSP samples compared to the unpeened samples. The corrosion rate is directly related to the corrosion current and can be extracted using the method described in Section 5.1.1. The corrosion rates are shown in *Figure 6.2*.

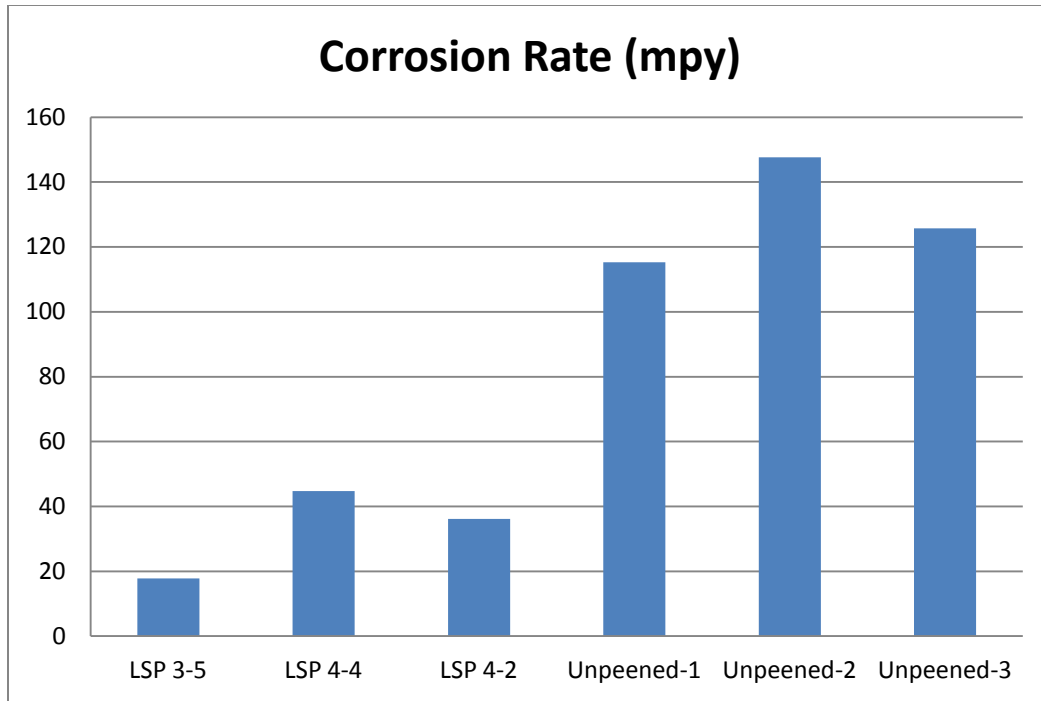


Figure 6.2 – DC polarization corrosion rates

Figure 6.2 shows a significant reduction in corrosion rate for the peened samples compared to the unpeened samples. This verifies the hypothesis that LSP is capable of decreasing the corrosion rate of magnesium and magnesium alloys. *Figure 6.3* shows a plot of in-plane compressive stress on the surface of the sample measured prior to being tested vs. the corrosion rate.

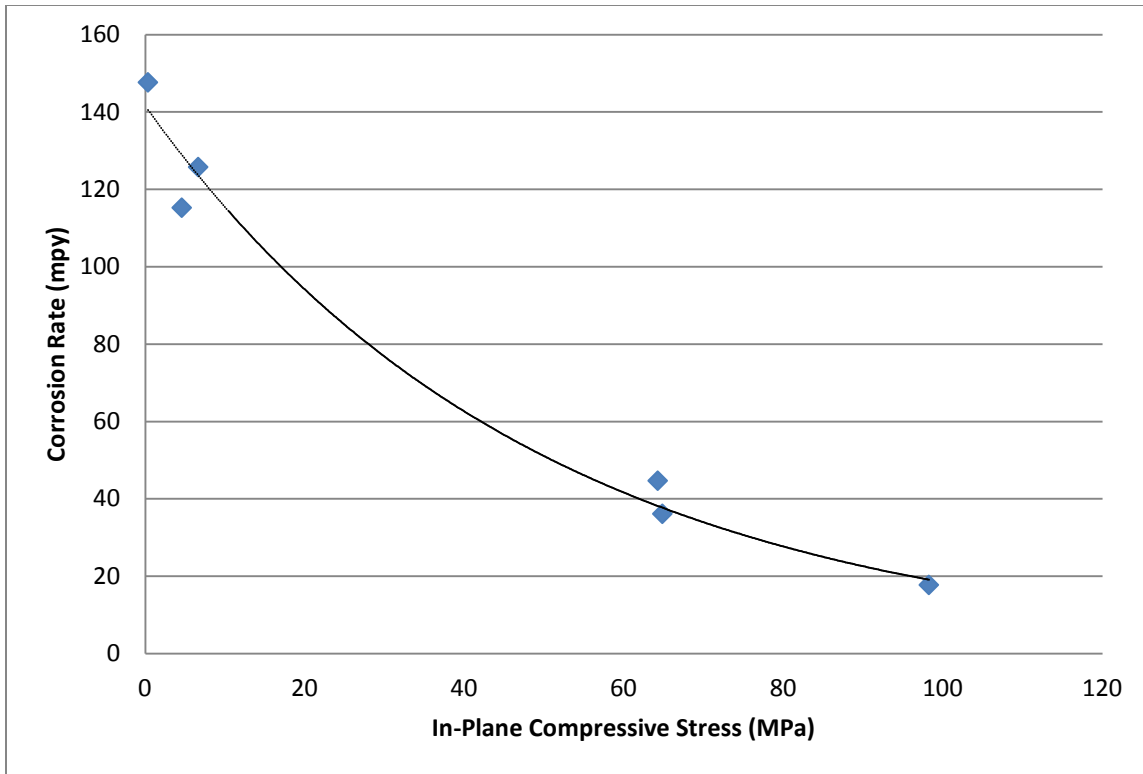


Figure 6.3 – In-plane compressive stress vs. corrosion rate

Figure 6.3 suggests that corrosion rate follows an exponentially decaying curve relating to the measured compressive stress on the surface of the material. However, it would take more data points to verify this trend. Since this thesis was meant to focus on many aspects of LSP magnesium alloy AZ91D, we will not verify this trend.

6.2 Immersion Test Results

Figure 6.4 shows the results of the immersion tests performed. The data shown provides inconclusive results from the immersion tests. Most LSP samples appear to have the same weight-loss measurements as the unpeened samples, while some LSP sample have increased weight loss. However, due to observations made during the test, it can be concluded that experimental errors and inconsistencies attributed to these results.

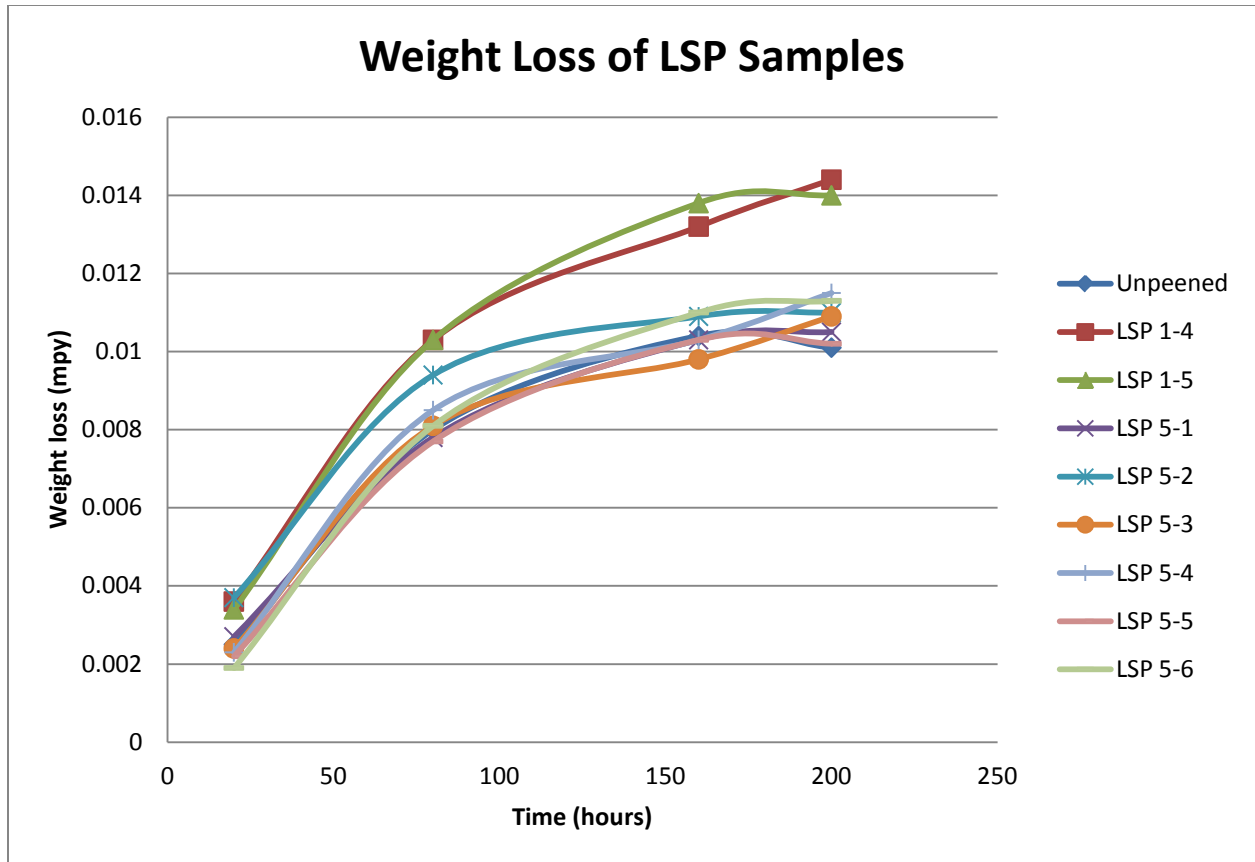


Figure 6.4 – Immersion test weight loss measurements

Difficulties arose during the immersion test that made it complicated to achieve accurate results. Since the weight-loss of the samples is very small over the immersion period compared to the total weight of the mounted sample, many factors can attribute to insufficient measurements.

During the immersion test, it was observed that hydrogen bubble pockets began to form around the perimeter of the non-conducting tape. This creates an issue because the hydrogen pockets can eliminate exposure to the corrosive fluid. It was also observed that the corrosive fluid was flowing into crevices between the mold and the exposed surface. This creates problems because it can add to the weight of the overall sample when the measurements are taken. Another issue that arose during weight loss measurements was that there was the

difficulty in completely drying the samples for each measurement. If the samples were not completely dry, any fluid that remained on the sample could add weight to it.

Due to the inconsistencies described above, it can be concluded that the immersion test results are inconclusive. Similar immersion tests were performed using conducting molds that gave some very encouraging results. However, due to inadequate stress measurements and the galvanic couple created by using conducting molds to mount the samples, it was determined that these results were inconclusive. Future work shall include measures to eliminate these errors and obtain accurate measurements.

Chapter 7: Discussions

From this study, it can be concluded that LSP has significant effects on the residual stress and subsequently corrosion rates of magnesium alloy AZ91D. Double-sided LSP is capable of producing compressive residual stresses on this material, but the reasons for this must be determined. It is also obvious that there are some improvements to the corrosion rates of the samples due to LSP, which require some explanation.

7.1 LSP Methods

Previous studies [2, 6, 18, 31] have investigated the use of LSP on different magnesium alloys. Each of these studies was successful in obtaining relatively high levels of compressive residual stress from single-sided LSP [2, 6, 18, 31]. Our investigation dedicated a significant amount of experimentation with single-sided LSP, but was unsuccessful in achieving compressive residual stresses on the surface of the materials. Some explanation for this discrepancy can be offered due to the inefficiency of the laser used for all LSP. During the experimentation with different single-sided peening methods, it was observed that the laser pulse durations were not consistently following the SRT peak followed by the Gaussian curve as described in Chapter 1 of this thesis. The pulse duration and temporal shape of the laser can have significant effects on the residual stresses achieved in the material.

The laser inefficiencies along with low material hardness compared to typical materials processed by LSP can also be offered as some explanation as to why only double-sided LSP worked for it. Millet et al. [32] conducted an experiment investigating the shock response of Mg alloy AZ61 in which 10 mm thick AZ61 plates were imbedded with stress gauges and were impacted with copper disks at pressures ranging from 1.24-8.20 GPa. It was concluded [32] that the material reached an elastic limit of 191.3 MPa at 10 mm from the impact surface. This

means that the material was likely experiencing some plastic deformation at even 10 mm from the impact surface. This can offer some explanation for why single-sided LSP on AZ91 is not resulting in significant compressive residual stress in that the pressure pulse is far exceeding its Huganiot Elastic Limit such that visible plastic deformation occurs at the surface, but no residual stresses are maintained. Since the material is so soft, the shock response from LSP travels through the material, creating some work hardening farther away from the LSP surface and likely leaving compressive residual stresses closer to the center of the specimen rather than near the surface.

7.2 Corrosion Tests

The DC polarization test is a good indication that LSP is capable of decreasing the corrosion rates of the material. However, successful implementation of the immersion test is typically a better indication of the true effects on the corrosion rate of the sample. A better method for the immersion test should include an LSP patch of overlapping shots across the entire test coupon and fully immersing the coupon in the corrosive fluid.

This is the first known study investigating the effects of laser shock peening on the corrosion rates of a magnesium-aluminum alloy. Guo and Sealy et al. [31] were able to successfully improve the corrosion rates of a magnesium-calcium alloy for use as a biodegradable material using LSP. In this experimentation [31], overlapping LSP shots were applied in different patterns to study the effects of the surface topography created from LSP on the corrosion rates tested through potentiodynamic tests in a Hank's balanced salt solution. It was concluded that the improvement in corrosion was attributed to the higher surface roughness from LSP and that 25% shot overlap gave the best results [31]. This is more confirmation that

overlapping shots should be investigated along with FEA modeling to determine the best method to obtain high compressive stresses at the surface.

Although the experimental data makes it difficult to observe significant microstructure changes due to LSP, it does create obvious mechanical improvements that can be attributed to the observed effects on the corrosion rate of the material. The compressive stresses and increase in hardness can be offered as valid explanations for the improvements on corrosion rates of the material. In previous studies, Peyre et al. [7] concludes that the mechanical modifications induced from LSP (residual stress and work hardening) on 316L stainless steel are the cause for improvement in corrosion rates. It is also suggested [7] that LSP and shot peening can reduce corrosion pit initiation by embedding surface inclusions (which can cause corrosion pitting) into a compressive stress field that can modify the structure of the inclusion interfaces.

Chapter 8: Conclusion and Future Work

This report detailed the effects of residual stress induced by LSP on magnesium alloy AZ91D on the corrosion rate of the material. The following can be concluded from this study:

- In order to accurately measure residual stresses and view a grain structure on AZ91D, the material must be annealed at about 420°C for a minimum of 24 hours. Annealing decreases the hardness, but increases XRD peaks and allows for accurate analysis of data.
- Significant compressive residual stress can be achieved through double-sided LSP. Residual stresses were observed between -60 and -180 MPa using double-sided LSP. Single-sided LSP did not result in significant compressive residual stress on the surface of the material. Laser inefficiencies, along with low material hardness are the likely causes the material not maintaining compressive RS on the surface from single-sided LSP. Stress-depth profiles from double-sided LSP reveal an immediate increase in compressive residual stress within 20 μm of the surface, then slowly increase and reach the tensile region between 400-600 μm . Double-sided LSP creates a shift to the right in the X-ray diffraction pattern peaks of the material, indication compressive RS. The laser used creates a relatively uniform dimple shape with dimple depths ranging from 25 to 100 μm , depending on the laser intensity. Double-sided LSP causes about a 15% increase in the micro-hardness of the material.
- The Johnson-Cook material model was successfully implemented in a Finite Element model in LS-DYNA to simulate the effects of LSP on the residual stress of AZ91D. The FEA model is capable of determining the residual stress depth profile, stress contour profiles, and material deformations from LSP. A variation study of the thermal energy

correction factor, α , indicates that a value of 1.0 is best for accurate simulations with the present laser in use.

- DC Polarization tests prove LSP can decrease corrosion rates from 2.5 to 8 times that of an unpeened sample. The decrease in corrosion rates measured can be attributed to the improvements in mechanical properties of the material due to LSP.
- Immersion test results were inconclusive due to inaccurate measurements results from issues with sample preparation, hydrogen pockets, and weight accumulation of the corrosive fluid.

Based on the current findings, the following is suggested for future work:

- Electron backscatter diffraction (EBSD) analysis should be performed before and after LSP to obtain accurate grain size measurements. More detailed residual stress analysis with LSP, including laser intensity vs. residual stress, more stress-depth profiles, and LSP overlapping patch analysis.
- Fatigue and Stress Corrosion Cracking (SCC) tests before and after LSP should be performed.
- Further FEA work can be done, including further material model parameter calibration with more residual stress results and an LSP patch study. A micro-scale material model can also be developed to more accurately capture the residual stress effects. A larger sample of data should be collected for both the immersion tests and DC polarization tests to validate any relationship between residual stress and corrosion rates.
- An immersion test should be performed in which a sample is peened with overlapping shots on all surfaces and fully immersed in the corrosive fluid to measure the true weight

loss of the sample. An immersion test with hydrogen generation measurements should be performed.

References

- [1] A. Weiler, *et al.*, "Biodegradable implants in sports medicine: The biological base," *Arthroscopy: The Journal of Arthroscopic & Related Surgery*, vol. 16, pp. 305-321, 2000.
- [2] Y. B. Guo and M. P. Sealy, "Surface integrity and process mechanics of laser shock peening of novel biodegradable magnesium-calcium (Mg-Ca) alloy," *Journal of the Mechanical Behavior of Biomedical Materials*, pp. 488-496, 2010.
- [3] J. F. Shi, *et al.*, "Design and Simulation of a Femoral Component Peg in Total Knee Replacement," *Key Engineering Materials*, vol. 450, pp. 111-114, 2011.
- [4] H. Weinans, *et al.*, "Sensitivity of periprosthetic stress-shielding to load and the bone density–modulus relationship in subject-specific finite element models," *Journal of Biomechanics*, vol. 33, 2000.
- [5] Y. B. Guo and M. P. Sealy, "Fabrication and Characterization of Surface Texture for Bone Ingrowth by Sequential Laser Peening Biodegradable Orthopedic Magnesium-Calcium Implants," *Journal of Medical Devices*, vol. 5, 2011.
- [6] Y. Zhang, Lu, Jinzhong, Cui, Chengyun, Jiang, Yingfang, Ren, Xudong, "Effects of laser shock precessing on stress corrosion cracking susceptibility of AZ31B magnesium alloy," *Surface and Coating Technology*, vol. 204, pp. 3947-3953, 2010.
- [7] P. Peyre, *et al.*, "Surface modifications induced in 316L steel by laser peening and shot-peening, Influence on pitting corrosion resistance," *Materials Science & Engineering*, vol. A280, pp. 294-302, 2000.
- [8] M. J. Grimm, "Biomedical Engineering Design Handbook: Orthopedic Biomaterials," pp. 421-444, 2009.
- [9] C. K. Seal, *et al.*, "Biodegradable Surgical Implants based on magnesium alloys: a review of current research," *IOP Conference Series: Material Science Engineering*, vol. 4, 2011.
- [10] M. P. Staiger, Pietak, A. M., Huadmai, J., and Dias, G., "Magnesium and Its Alloys as Orthopedic Biomaterials: A Review," *Journal of Biomaterials*, vol. 27, pp. 1728-1734, 2006.
- [11] G. Song., "Control of Biodegradation of Biocompatible Magnesium Alloys," *Corrosion Science*, vol. 49, pp. 1696-1701, 2007.
- [12] F. Witte, "The history of Biodegradable Magnesium Implants: a review," *ActaBiomaterialia*, pp. 1680-1692, 2010.
- [13] G. Song, Song, S., , *Acta Phys.-Chim. Sin.*, p. 1222, 2006.
- [14] J. Chen, Ai, M., Wang, J., Han, E.H., Ke, W., "Stress Corrosion Cracking Behaviors of AZ91 Magnesium Alloy in Deicer Solutions using Constant Load," *Materials Science and Engineering A*, vol. 515, pp. 79-84, 2009.
- [15] N. Winzer, Atrens, A., Dietzel, W., Song, G., Kainer, K.U., "Stress Corrosion Cracking (SCC) in Mg-Al Alloys Studied using Compact Specimens," *Advanced Engineering Materials*, vol. 10, 2008.
- [16] C. S. Montross, Wei, T., Yi, L., Clark, G., Mai, Y.W, "Laser shock processes and its effects on microstructure and properties of metal alloys: a review," *International Journal of Fatigue*, vol. 24, pp. 1021-1036, 2002.
- [17] J. Hu, Lou, J., Shen, H., Wu, S., Chen, G., Huang, K., Ye, L., Liu, Z., Shi, Y., Yin, S., "The effects of laser shock peening on microstructure and properties of metals and alloys: a review," *Advanced Materials Research*, vol. 347-353, pp. 1596-1604, 2011.
- [18] S. Huang, Zhou, J.Z., Jiang, S.Q., Yang, X.D., Wang, C.D., Dai, Y.C., "Experimental Study on Laser Shock Peening of AZ31B Magnesium Alloys Sheet," *Materials Science Forums*, vol. 628-629, pp. 691-696, 2009.
- [19] R. M. White, "Elastic Wave Generation by Electron Bombardment or Electromagnetic Wave Absorption," *Journal of Applied Physics*, vol. 34, pp. 2123-2124, 1963.

- [20] J. E. Michaels, "Thermal impact--the mechanical response of solids to extreme electromagnetic radiation," *Planetary and Space Science*, vol. 7, p. 427, 1961.
- [21] N. C. Anderholm, "Laser-Generated Stress Waves," *Applied Physics Letters*, vol. 16, p. 113, 1970.
- [22] A. Gordon, "Systematic Modeling of the Laser Shock Peening Process with Applications to Residual Stress and Damage Prediction," 2010.
- [23] D. Devaux, R. Fabbro, L. Tollier, E. Bartnicki, "Generation Of Shock-Waves By Laser-Induced Plasma In Confined Geometry," *Journal Of Applied Physics*, vol. 74, pp. 2268-2273, 1993.
- [24] K. N. Braszczynska-Malik, "Precipitates of Υ_2 -Mg₁₇Al₁₂ Phase in AZ91 Alloy, Magnesium Alloys – Design, Processing and Properties," *Institute of Materials Engineering*, 2009.
- [25] M. Janes, "Product Data," J. Russo, Ed., ed: ACT Test Panels, 2011.
- [26] R. Fabbro, J. Fournier, P. Ballard, D. Devaux, and J. Virmont, "Physical Study Of Laser-Produced Plasma In Confined Geometry," *Journal of Applied Physics*, vol. 68, pp. 775-784, 1990.
- [27] L. Schwer. *Optional Strain-Rate Forms for the Johnson Cook Constitutive Model and the Role of the Parameter Epsilon_0*.
- [28] I. Ulacia, Salisbury, C.P., Hurtado, I., Worswick, M.J., "Tensile characterization and constitutive modeling of AZ31B magnesium alloy sheet over wide range of strain rates and temperatures," *Journal of Materials Processing Technology*, vol. 211, pp. 830-839, 2011.
- [29] M. Caldwell, "Corrosion and Electrochemistry Experts," *Electrochemistry*, 2008.
- [30] D. Enos, Scribner, Louie,, "The Potentiodynamic Polarization Scan," *Center for Electrochemical Science & Engineering*, 1997.
- [31] Y. B. Guo, Sealy, Michael P., Guo, Changsheng, "Significant improvement of corrosion resistance of biodegradable metallic implants processed by laser shock peening," *CIRP Annals - Manufacturing Technology*, vol. 61, pp. 583-586, 2012.
- [32] J. C. F. Millett, Stirk, S.M., Bourne, N.K., Gray, G.T. III, "On the behaviour of the magnesium alloy, AZ61 to one-dimensional shock loading," *Acta Materialia*, vol. 58, pp. 5675-5682, 2010.